

## Proiect 1. Caracterizarea mecanică a materialelor celulare și a structurilor sandwich cu miez din materiale celulare folosite la fațade inteligente

Parteneri:      Universitatea Politehnică Timișoara (Coordonator)  
                     Universitatea Tehnică de Construcții București, UTCB (P1)  
                     Universitatea Tehnică Cluj Napoca (P2)

### Determinarea proprietăților mecanice ale materialelor celulare folosite ca izolații ale fațadelor inteligente, prin încercări mecanice de compresiune, încovoiere, etc.

Panourile sandwich sunt folosite pe scara largă pe piața de construcții din România pentru realizarea acoperisurilor și peretilor de închidere. Fiecare producător oferă tabele cu capacități portante în scopuri de proiectare, însă, în multe cazuri au fost evidențiate diferențe foarte mari între capacitățile portante declarate între diferiți producători și rezultatele încercărilor experimentale efectuate pe panouri, deși acestea prezentau detalii tehnice similare precum grosimea interioară sau exterioară a fețelor sau grosimea miezului. (Szolt, 2015).

În continuare sunt prezentate materialele folosite de cinci producători din România, pentru realizarea panourilor sandwich, Tab.1.

**Tabelul 1** Tipuri de panouri tip sandwich

<b>Catalog Joris ide- Materiale folosite la panouri sandwich</b>			
Destinație	Miez	Placa interioara/exterioara	
Acoperis	PUR/PIR la cerere	Tabla otel S 250 GD	<p>Vă rugăm indicați lungimea panourii și grosimea tablăi.          Lungime minimă tablă: 2,50m          Lungime maximă panou: 11,5m          Încovoiere: Max. 50mm (standard)          max. 100mm</p>
	Vata minerala	Tabla otel S 250 GD	
Acoperis/perete	PIR	Hartie Kraft sau folie aluminiu	
Perete	PUR/PIR la cerere	Tabla otel S 250 GD	
	Vata minerala	Tabla otel S 250 GD	

<b>Catalog Kingspan- Materiale folosite la panouri sandwich</b>			
Destinație	Miez	Placa interioara/exterioara	
Acoperis	IPN/PUR	Otel	<p>1,000 mm – lățimea tablăi</p> <p>250 mm    250 mm    250 mm    250 mm</p> <p>Profilare interioară</p> <p>B (box)      MB (minibox)</p>
	PIR	Otel Fe 220G	
	IPN/PUR	Membrana bituminoasa	
	IPN/PUR	Fibra de sticla	
	IPN/PUR	Membrana PVC	
	Fibra minerala	Otel + membrana PVC	

Perete	PUR/PIR la cerere	Tabla otel	
	Vata minerala	Tabla otel	

### Catalog **Isopan**- Materiale folosite la panouri sandwich

Destinatie	Miez	Placa interioara/exterioara	
Acoperis	PUR	Tabla otel	
	PUR	Tabla aluminiu	
	PUR	Folie gofrata aluminiu	
	PUR	Suport din carton bituminat	
	Vata minerala	Tabla otel	
Perete	PUR	Tabla otel	
	Vata minerala	Tabla otel	

### Catalog **Topanel**- Materiale folosite la panouri sandwich

Destinatie	Miez	Placa interioara/exterioara	
Acoperis	PUR/PIR	Tabla otel	
	PUR/PIR	Tabla aluminiu	
	PUR	Rasina poliesterica armata cu fibra de sticla	
	PUR	Carton bituminat	
	Vata minerala	Tabla otel	
Perete	PUR	Tabla otel	
	Vata minerala	Tabla otel	

### Catalog **Marcegaglia**- Materiale folosite la panouri sandwich

Destinatie	Miez	Placa interioara/exterioara	
Acoperis	PUR	Tabla otel	
	PUR	Tabla cupru	
	PUR	Tabla aluminiu	

	PUR	Carton bituminat Folie de aluminiu	
	PUR	Fibra de sticla	
	Vata minerala bazaltica	Tabla otel	
Perete	PUR	Tabla otel	
	PUR	Tabla aluminiu	
	PUR	Fibra de sticla PRFV	
	Vata mineral bazaltica	Tabla otel	

### Clasificare și proprietăți ale materialelor folosite ca fețe/miezuri

Au fost folosite urmatoarele materiale pentru:

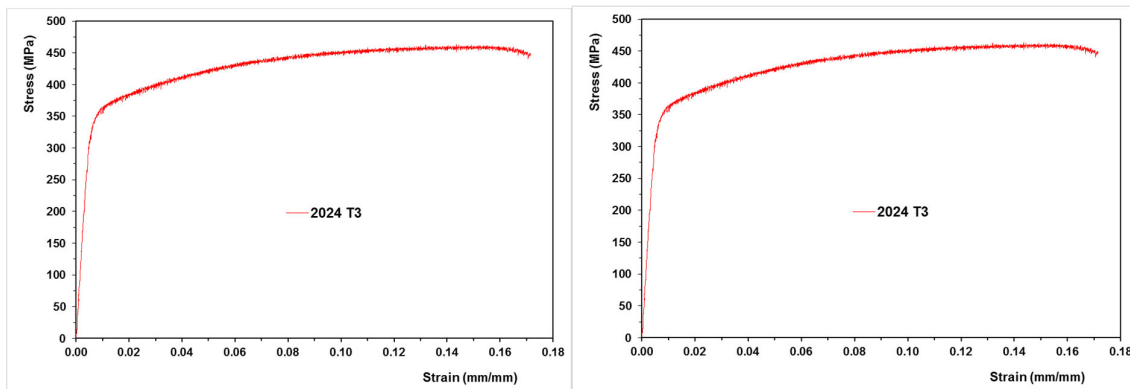
- **fețe:** Aluminiu (AL 2024 T3; AL 6060 T66; AL 1050 H24), material textil, PVC, Tabla expandata din otel inoxidabil;
- **miez:** spuma: Polyisocianurat (PIR), Poliuretanică Rigida (PUR) cu celule închise, Metalica de aluminiu (MF) cu celule închise, Polistirenul Expandat (EPS).

Pe acestea s-au efectuat incercari de **tractiune** (fețe) pe epruvete de tip dogbone, de tip banda, prismatice, folosindu-se ca echipament: Mașină de încercat universală Zeick Proline Z005 (AL 2024 T3; AL 6060 T66) la viteza de incercare  $v=5$  mm/min, Masina de testat Walter+bai LFV 100 (AL 1050 H24) la viteza de incercare  $v=10$  MPa/min Masina de tractiune-compresiune Zwick/Roel 005 (tabla expandata, PVC) la viteza de incercare  $v=10$  mm/min, la temperatura ambianta.

In continuare sunt prezentate rezultatele incercarilor de **tractiune** cu curbele caracteristice, pentru fiecare din materialele mentionate mai sus:

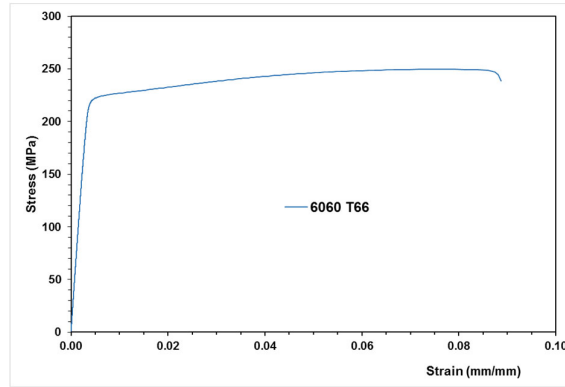
#### Aluminiu (AL 2024 T3; AL 6060 T66; AL 1050 H24)

Curbe caracteristice:



a. AL 2024 T3

b. AL 6060 T66



c.AL 1050 H24

Fig. 1 Curbele forta-deplasare la tractiune pentru

**Tabelul 2.** Proprietăți ale aliajelor de aluminiu folosite drept fețe

<b>AL 2024 T3</b>					
	<b>E (MPa)</b>	<b>R<sub>p0.2</sub> (MPa)</b>	<b>R<sub>m</sub> (MPa)</b>	<b>e<sub>m</sub> (%)</b>	<b>e<sub>f</sub> (%)</b>
1	70170	338.5	463.06	14.36	17.15
2	69270	332.7	446.26	14.48	16.61
3	70560	347.3	467.68	15.14	16.87
Average	<b>70000</b>	<b>339.5</b>	<b>459.0</b>	<b>14.66</b>	<b>16.88</b>

<b>AL 6060 T66</b>					
	<b>E (MPa)</b>	<b>R<sub>p0.2</sub> (MPa)</b>	<b>R<sub>m</sub> (MPa)</b>	<b>e<sub>m</sub> (%)</b>	<b>e<sub>f</sub> (%)</b>
1	68180	195.2	220.92	7.11	7.64
2	68510	221.9	249.6	7.73	7.73
3	70100	234.2	240.51	7.09	7.09
Average	<b>68930</b>	<b>217.1</b>	<b>237.0</b>	<b>7.31</b>	<b>7.49</b>

<b>AL 1050 H24</b>					
	<b>E (MPa)</b>	<b>R<sub>p0.2</sub> (MPa)</b>	<b>R<sub>m</sub> (MPa)</b>	<b>e<sub>m</sub> (%)</b>	<b>e<sub>f</sub> (%)</b>
1	70200	98.3	105.52	2.33	3.21
2	69870	97.3	105.78	2.59	3.68
3	71130	99.6	107.04	2.26	2.89
Average	<b>70400</b>	<b>98.4</b>	<b>106.1</b>	<b>2.39</b>	<b>3.26</b>

## Material textil

Curbe caracteristice:

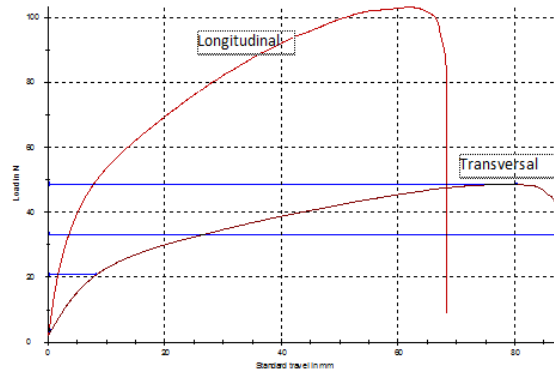


Fig. 2 Curbele tensiune-deformație la tracțiune.  
Influența direcției de încărcare

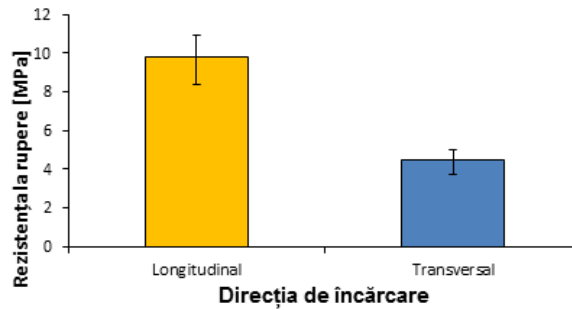


Fig. 3 Rezistența la rupere în funcție de direcția de încărcare

Concluzii:

- Rezistența la rupere este de 2,18 ori mai mare pe direcție longitudinală (9,79 MPa) comparativ cu direcția transversală (4,48 MPa).

## PVC

Curbe caracteristice:

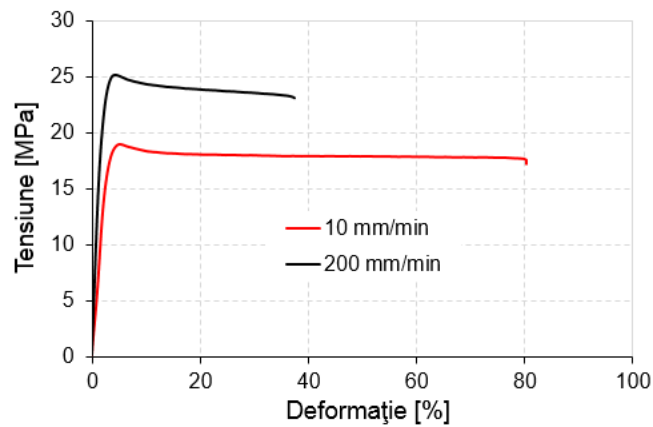


Fig. 4 Curbele tensiune-deformație la tracțiune.  
Influența vitezei de încărcare

Concluzii:

- Rezistența la rupere a fetelor din PVC este influențată de viteza de încercare. S-a obținut o creștere a rezistenței cu până la 25% în cazul unei viteze de testare de 200 mm/min (Figura 4).
- Pe de altă parte, alungirea la rupere este de două ori mai mare în cazul vitezei de încercare de 10 mm/min, comparativ cu 200 mm/min.

### *Tabla expandată din oțel inoxidabil*

Curbe caracteristice:

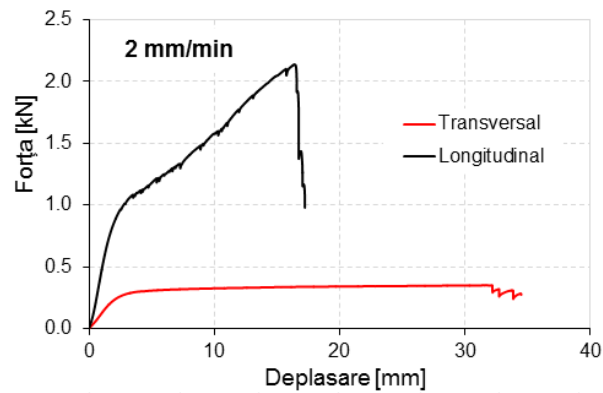


Fig. 5 Curbele forta-deplasare la tractiune.  
Influenta directiei de incarcare pentru 2 mm/min

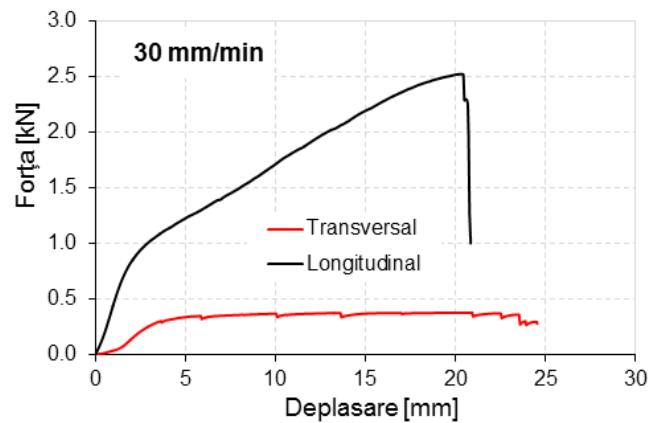


Fig. 6 Curbele forta-deplasare la tractiune.  
Influenta directiei de incarcare pentru 30 mm/min

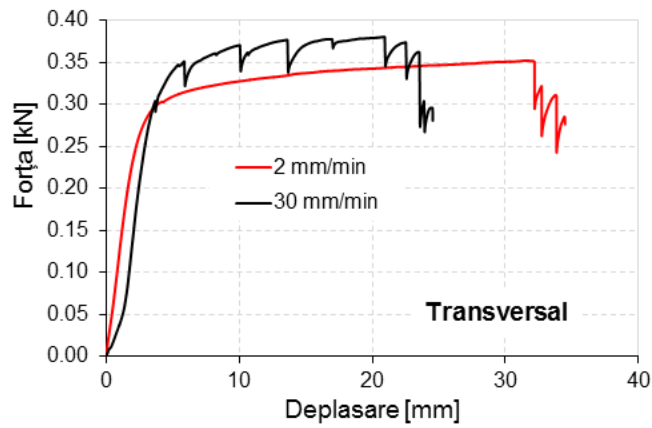


Fig. 7 Curbele forta-deplasare la tractiune.  
Influenta vitezei de incarcare pentru directia transversala

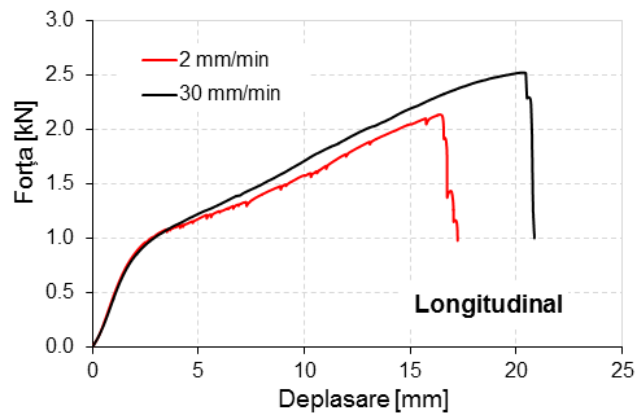


Fig. 8 Curbele forta-deplasare la tractiune.  
Influenta vitezei de incarcare pentru directia longitudinala

Concluzii:

- Directia de incarcare influenteaza major forta maxima a epruvetelor investigate. Astfel, directia longitudinala prezinta o imbunatatire cu pana la 83.9 pentru o viteza de incarcare de 2 mm/min (vezi Figura 5), aceasta crescand la 85.4% pentru 30 mm/min (vezi Figura 6).
- De asemenea, viteza de incarcare influenteaza forta maxima cu pana la 9.2% pentru directia transversala (vezi Figura 7) si cu 17.7% pentru directia longitudinala (vezi Figura 8).

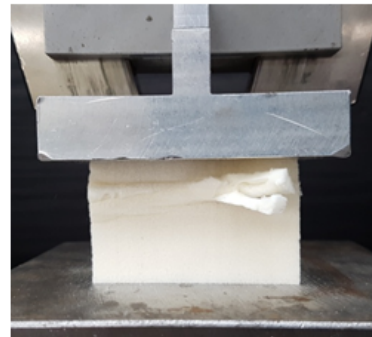
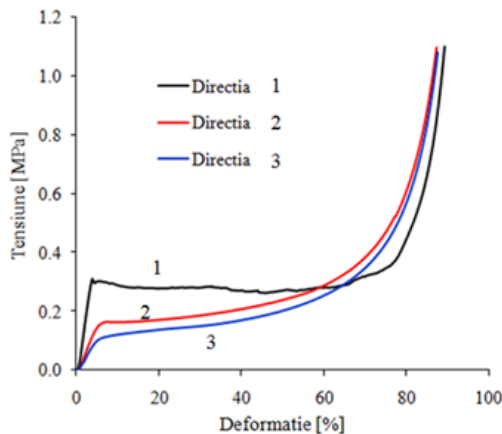
Materialele pentru miez au fost suspuse la **compresiune** (spuma PIR, PUR, MF, polistiren expandat) si **incovoiere in trei puncte** (PUR, MF, polistiren expandat EPS).

Pentru incercarea la **compresiune** au fost folosite epruvete cubice de dimensiune: 25x25x25 (PIR, PUR), epruvete cilindrice de dimensiune:  $D=25 \text{ mm} \times h=25 \text{ mm}$ , prisme de dimensiuni: 50x50x25. Pentru realizarea incercarilor s-a folosit urmatorul echipament: masina de incercat universala Zwick proline Z005 (PIR) la viteza  $v=10 \text{ mm/min}$ , masina de tractiune-compresiune LBG TC100, avand capacitatea maxima a celulei de forta de 100 kN (PUR, MF) la viteza  $v=10 \text{ mm/min}$ , masina de incercat universală tip Instron 3366 – 10 kN (EPS) la viteze de incercare: 15 mm/min, 75 mm/min, 225 mm/min și 375 mm/min, la o temperatura ambianta.

In continuare sunt prezentate rezultatele incercarilor de **compresiune** cu curbele caracteristice, pentru fiecare din materialele mentionate mai sus:

### **Spuma Polyisocianurat (PIR)**

Curbe caracteristice:



a. Curbe caracteristice tensiune - deformatie b. cedări ale spumei la încărcarea pe direcția 1

Fig. 9 Comportarea la compresiune a spumelor

Concluzii:

- Valorile caracteristicilor mecanice  $E$ ,  $\sigma_y$ ,  $\sigma_p$  sunt superioare pe direcția 1 comparativ cu cele pe direcțiile 2 și 3 de aproximativ 3 ori pentru modulul de elasticitate, respectiv de 2 ori valorile tensiunilor de curgere și paltou. De asemenea palierul de curgere este mai extins pe direcția 1.



## Spuma Poliuretanică Rigida (PUR) cu celule închise

Temperatura de testare: -20 – 100°C

Curbe caracteristice:

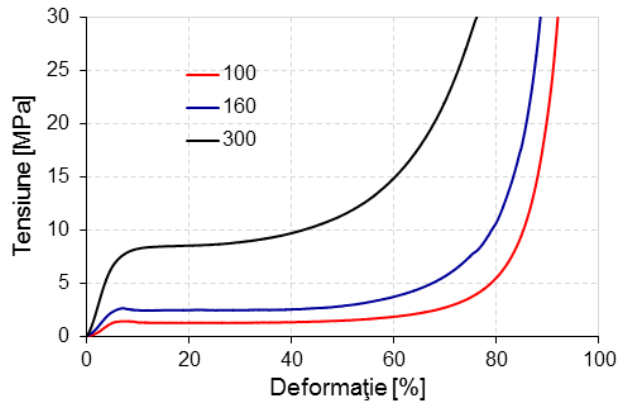


Fig. 10 Curbele tensiune-deformație la compresiune. Influența densității

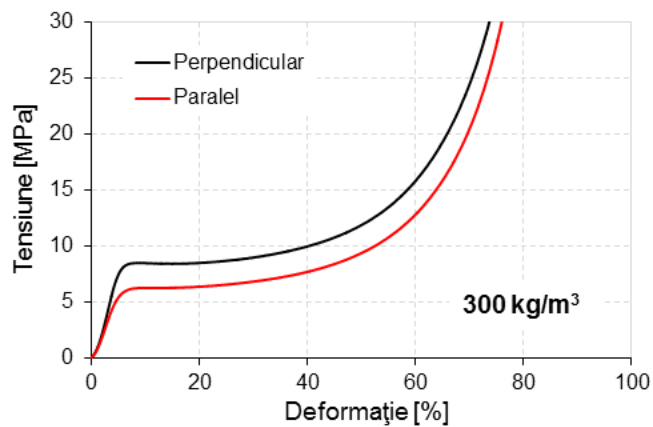


Fig. 11 Curbele tensiune-deformație la compresiune. Influența anizotropiei

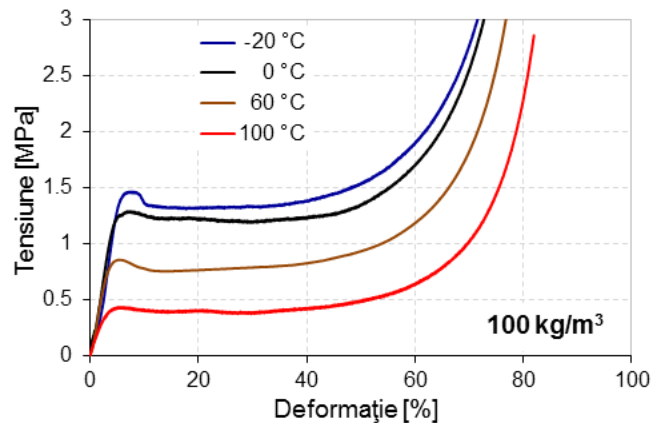


Fig. 12 Curbele tensiune-deformație la compresiune. Influența temperaturii

Concluzii:

- Principalele proprietăți mecanice (modulul de elasticitate, tensiunea de curgere, tensiunea de platou, densificarea și energia de absorbție) **cresc odată cu creșterea densității spumelor**

(Figura 10). Astfel, s-au observat creșteri a proprietăților elastice și de rezistență cu până la 86% la temperaturi joase ( $-20^{\circ}\text{C}$ ), respectiv 65% la temperaturi înalte ( $100^{\circ}\text{C}$ ).

- Direcția de încărcare evidențiază **comportamentul anizotrop** al spumelor investigate (Figura 11). Proprietățile mecanice ale spumelor testate într-un plan perpendicular pe planul de formare prezintă valori mai mari cu până la 40%, comparativ cu spumele încărcate într-un plan paralel cu planul de formare.
- **Temperatura influențează semnificativ** valorile proprietăților mecanice, acestea scăzând (cu până la 65% în intervalul de temperaturi investigat) odată cu creșterea acesteia (Figura 12).
- O parte dintre rezultatele obținute la caracterizarea spumelor poliuretanică au fost diseminate la conferința European Conference on Fracture 2018 la Belgrad, Serbia și publicate în Proceedings Structural Integrity.

### Spuma Metalică de aluminiu (MF) cu celule închise

Temperatura de testare:  $20 - 550^{\circ}\text{C}$

Curbe caracteristice:

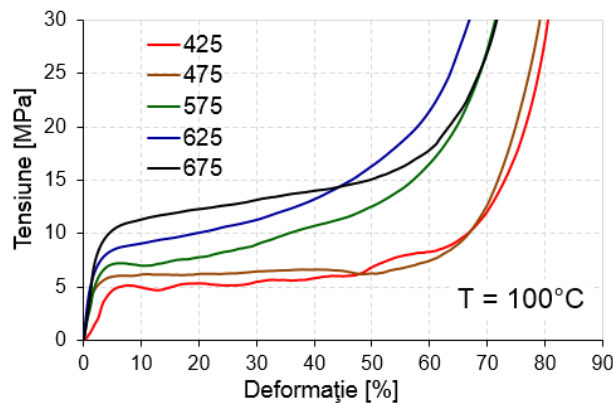


Fig. 13 Curbele tensiune-deformație la compresiune. Influența densității

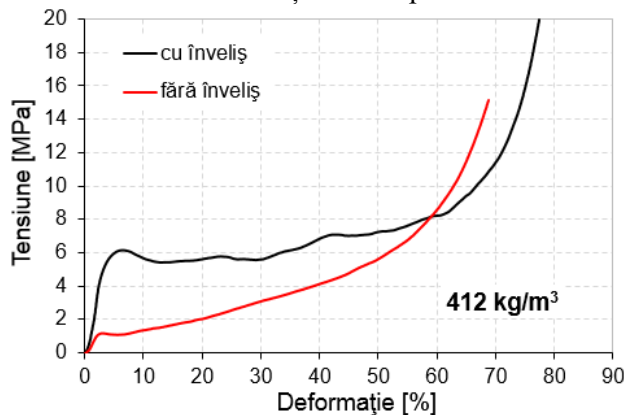


Fig. 14 Curbele tensiune-deformație la compresiune. Influența învelișului

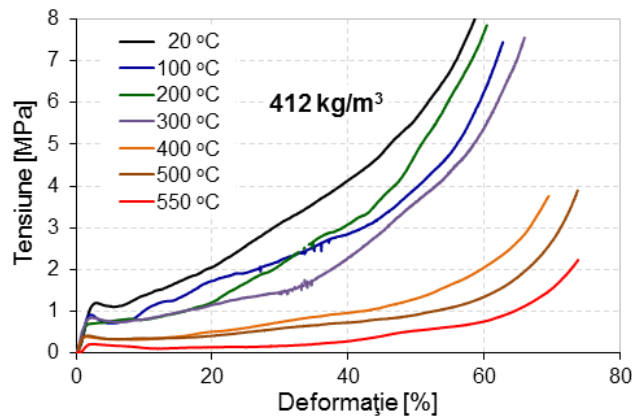


Fig. 15 Curbele tensiune-deformație la compresiune. Influenta temperaturii

Concluzii:

- Proprietățile mecanice *cresc odată cu creșterea densității* spumelor metalice cu pana la 52% (Figura 13).
- Învelișul exterior al epruvetelor influențează cu pana la 81% principalele proprietăți mecanice (Figura 14).
- *Temperatura influențează* rezistența mecanică a spumelor metalice cu pana la 85%, iar energia de absorbție cu aproximativ 90% (Figura 15). Toate proprietățile scad odată cu creșterea temperaturii de testare.
- Rezultatele privind proprietățile mecanice ale spumelor de aluminiu au fost publicate în jurnalul Materials.

#### *Polistirenul Expandat (EPS: EPS-50, EPS-80, EPS- 100, EPS- 120)*

Pentru încercarea la compresiune s-au folosit epruvete cu dimensiunile 50/50/25 [mm] (a se vedea Fig. 16).

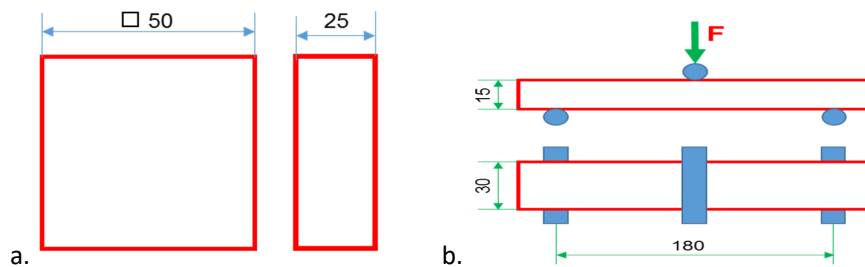


Fig. 16 Epruvete din polistiren expandat pentru solicitări la compresiune (a), respectiv încovoiere (b)

Curbe caracteristice:

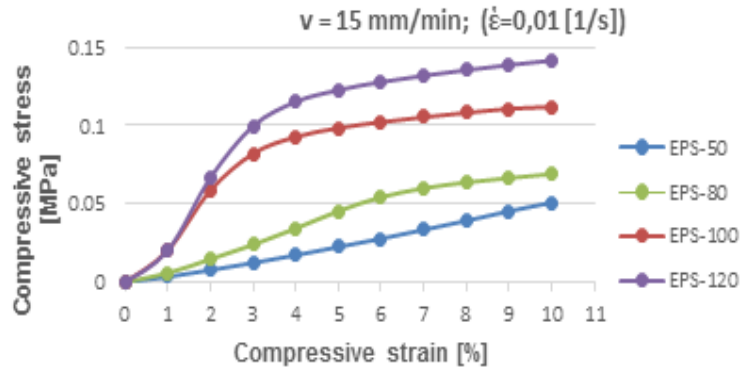


Fig. 17 Curba la compresiune pentru  $v=15\text{mm/min}$

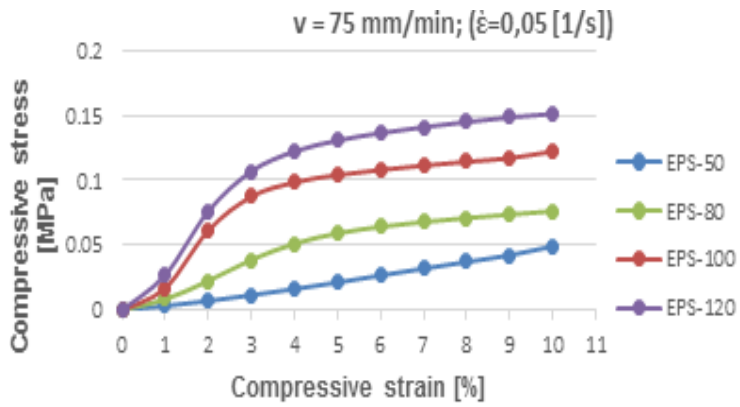


Fig. 18 Curba la compresiune pentru  $v=75\text{mm/min}$

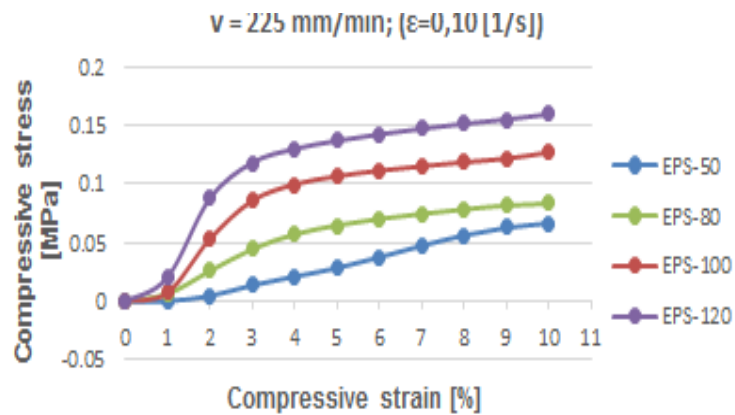


Fig. 19 Curba la compresiune pentru  $v=225\text{mm/min}$

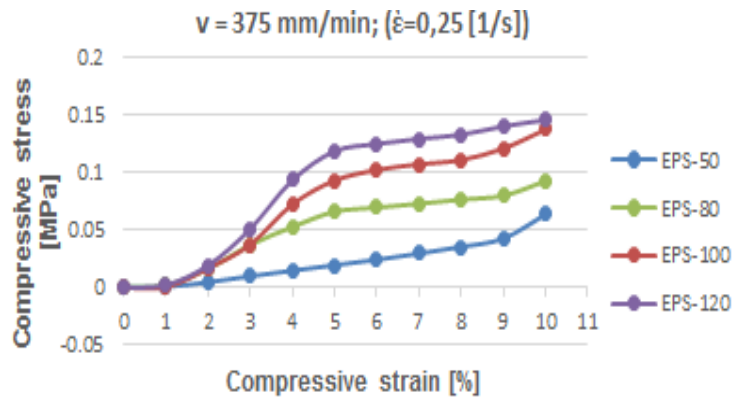


Fig. 20 Curba la compresiune pentru  $v=375\text{mm/min}$

**Tabelul 3.** Rezistenta la compresiune pentru tipurile de polistiren investigate la diverse viteze de încercare

$\sigma$ [kPa]				$v$ [mm/min]	$\dot{\epsilon}$ [1/s]
EPS-50	EPS-80	EPS-100	EPS-120		
53,38	70,55	111,9	138,14	15	0,01
55,96	81,10	122,39	148,24	75	0,05
60,15	84,88	128,14	156,32	225	0,10
69,79	92,72	133,62	145,8	375	0,25

Pentru spumele de polistiren s-a încercat o predicție analitică a comportării acestora pornind de la modelele micromecanice de estimare a curbei tensiune - deformare pentru EPS este necesară și de dorit pentru analiza structurală și aplicațiile de proiectare ale EPS. După cum se poate vedea din figurile 2 - 5, curba tensiune - deformare a EPS sub compresiune uniaxială are caracteristici geometrice diferite, care pot fi date matematic după cum urmează:

- etapa inițială de încărcare caracterizată printr-o relație liniară între tensiune și deformare, coeficientul de proporționalitate fiind echivalent cu modulul de elasticitate (modulul tangent):

$$\sigma_e = m * \epsilon \quad (1)$$

- zona platoului și zona de densificare pot fi descrise printr-o lege a puterii care include efectul ratei de deformare:

$$\sigma_p = k * \epsilon^a * \left(\frac{\dot{\epsilon}}{\dot{\epsilon}_0}\right)^b \quad (2)$$

$$\dot{\epsilon}_0 = \frac{v}{h_0} \quad (3)$$

$$\dot{\epsilon} = \frac{v}{h_i} \quad (4)$$

$$h_i = h_0 - \Delta h \quad (5)$$

$$\Delta h = h_0 * x\% \quad (6)$$

- (1) - ecuație pentru domeniul proporționalității (aria elastică).
- (2) - ecuație pentru domeniul plastic.
- (3) - rata de deformare, în raport cu viteza de testare ( $v = \text{mm} / \text{min}$ ) și înălțimea inițială a probei ( $h_0 = 25\text{mm}$ ).
- (4) - rata de deformare, în raport cu viteza de încercare ( $v = \text{mm} / \text{min}$ ) și înălțimea „hi” ( $h_i = \text{mm}$ ).
- (5) - „hi” reprezintă diferența dintre înălțimea inițială și deplasarea.
- (6) - „x” reprezintă procentul de deplasare.

Pentru EPS cu densități diferite și încărcate la diferite rate de deformare, coeficienții modelului m, k, a și b sunt prezentați în tabelul 1.

**Tabelul 4.** Coeficienții modelelor micromecanice

Densitate [kg/m <sup>3</sup> ]	Viteza de testare [mm/min]							
	15	75	15	75	15	75	15	75
	Coeficienți							
	m		k		a		b	
11	1,16	1,16	0,1	0,1	0,2	0,25	0,9	0,95
15	1,16	1,16	0,1	0,1	0,2	0,2	0,85	0,85
20	1,16	2,1	0,1	0,13	0,17	0,1	0,92	0,9
25	2,5	2,5	0,15	0,16	0,1	0,1	0,85	0,85

În continuare sunt prezentate curbele experimentale și cele teoretice obținute la încercarea de compresiune a polistirenului, pentru vitezele de testare  $v=15\text{mm/min}$  și  $v=75\text{mm/min}$ .

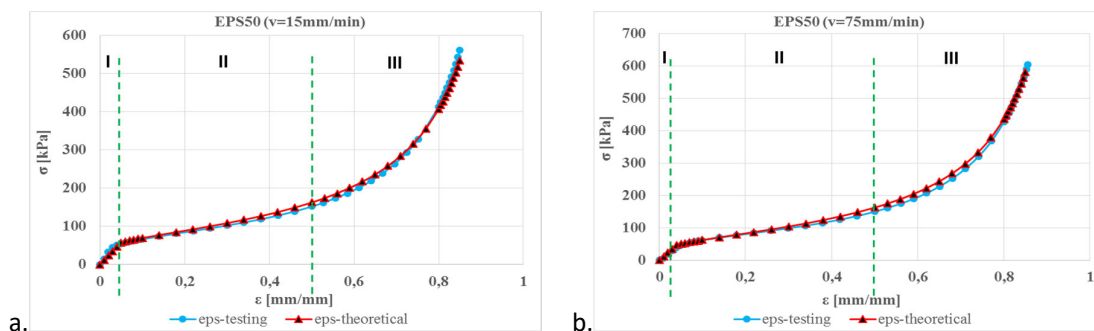


Fig. 21 Polistiren expandat EPS 50 încărcat la diferite rate de deformare (viteză transversală):  
a.  $v=15\text{mm/min}$ , b.  $v=75\text{mm/min}$

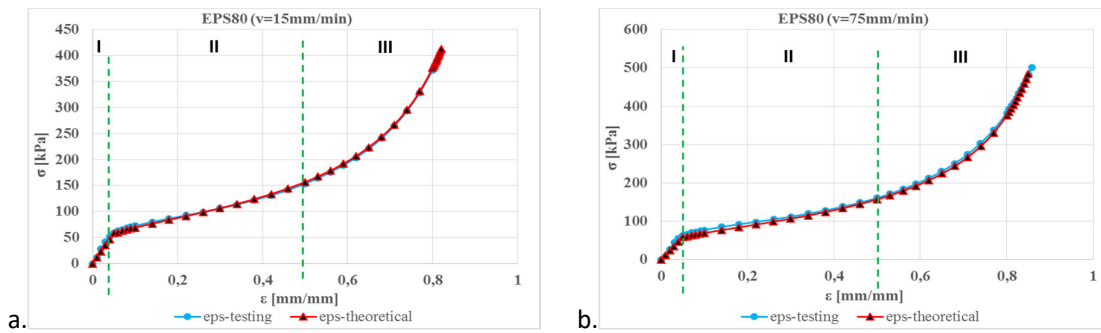


Fig. 22 Polistiren expandat EPS 80 încărcat la diferite rate de deformare (viteză transversală):  
a.  $v=15\text{mm/min}$ , b.  $v=75\text{mm/min}$

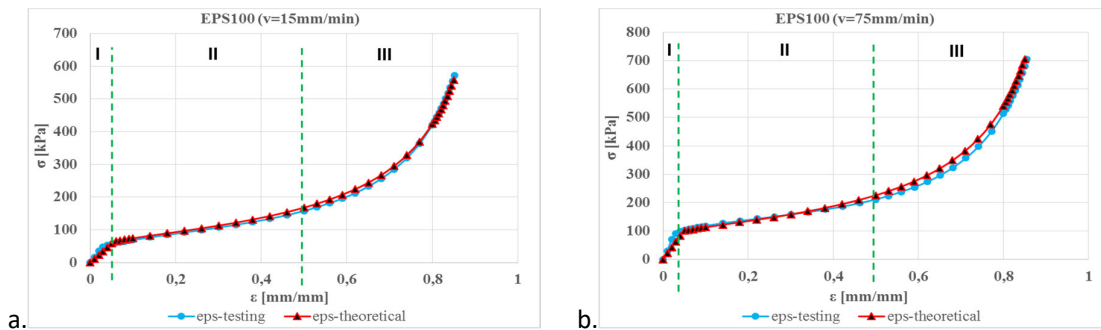


Fig. 23 Polistiren expandat EPS 100 încărcat la diferite rate de deformare (viteză transversală):  
a.  $v=15\text{mm/min}$ , b.  $v=75\text{mm/min}$

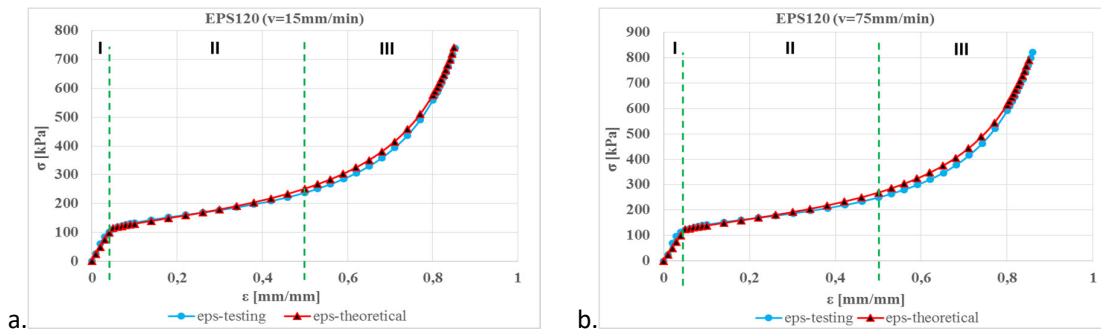


Fig. 24 Polistiren expandat EPS 120 încărcat la diferite rate de deformare (viteză transversală):  
a.  $v=15\text{mm/min}$ , b.  $v=75\text{mm/min}$

În graficele prezentate mai sus se pot observa trei intervale ale curbelor obținute la compresiune, atât pentru cele experimentale (curba albastră) cât și pentru cele determinate teoretic (curba roșie). Primul interval (I) reprezintă o zonă de proporționalitate în care rezistența la compresiune crește proporțional cu deformația. Această zonă proporțională este de până la 5% din deformație, (așa cum se poate vedea în figurile 21-24.

Iar al doilea interval (II) respectiv al treilea interval (III) reprezintă o zonă de palier urmată de o creștere accentuată a rezistenței la compresiune.

## Concluzii:

- În timpul testelor de compresiune a polistirenului expandat, s-a observat o influență a vitezei de încercare asupra rezistenței mecanice a acestuia.
- Se poate observa că regiunea elastică liniară se termină la atingerea tensiunii de platoului. În regiunea platoului, tensiunea rămâne aproape constant pe întregul interval. Când se atinge tensiunea de densificare, tensiunea crește brusc datorită compactărilor celulare sau densificării.
- Dependența de rata de deformare a polistirenului expandat este atribuită proprietăților viscoelastice ale materialului de bază, sau ruperii celulelor, mecanismelor de blocare care pot apărea între celulele adiacente deformante și mișcarea aerului în interiorul structurii.
- Modelul matematic propus de tensiune - deformare a fost validat cu rezultatele testelor și ar putea fi utilizat pentru proiectarea structurii și analiza structurală a EPS.

La **încovoierea în trei puncte** au fost folosite epruvete prismatice fara crestatura: 25 mm × 25 mm × 150 mm (PUR), 10 mm × 10 mm × 85 mm (MF), 15x30x180 (EPS). Pentru realizarea încercărilor s-a folosit următorul echipament: mașina de tractiune-compresiune Zwick/Roel 005, la viteza  $v = 2$  mm/min (PUR) și  $v = 10$  mm/min (MF), mașina de încercat universală tip Instron 3366 - 10KN (EPN) la vitezele de încercare: 15 mm/min, 75 mm/min, 225 mm/min și 375 mm/min, la temperatura ambiantă.

În continuare sunt prezentate rezultatele încercărilor de **încovoiere în trei puncte** cu curbele caracteristice, pentru fiecare din materialele menționate mai sus:

### *Spuma Poliuretanică Rigidă (PUR) cu celule închise*

Curbe caracteristice:

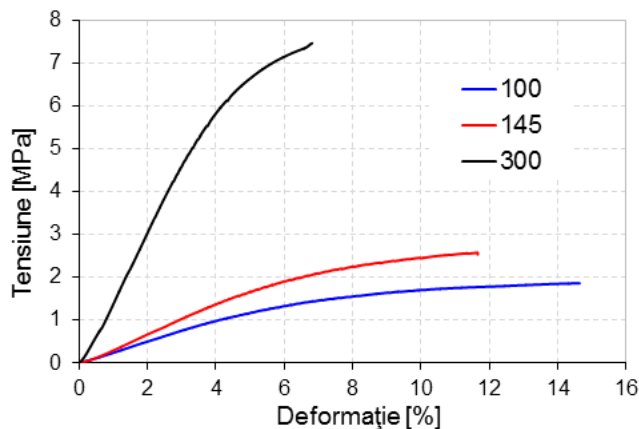


Fig. 25 Curbele tensiune-deformație la încovoiere în trei puncte. Influența densității

## Concluzii:

- Proprietățile elastice cresc cu 85% odată cu creșterea densității spumei, iar cele de rezistență cu aproximativ 75% (Fig. 25).



## Spuma Metalica de aluminiu (MF) cu celule închise

Curbe caracteristice:

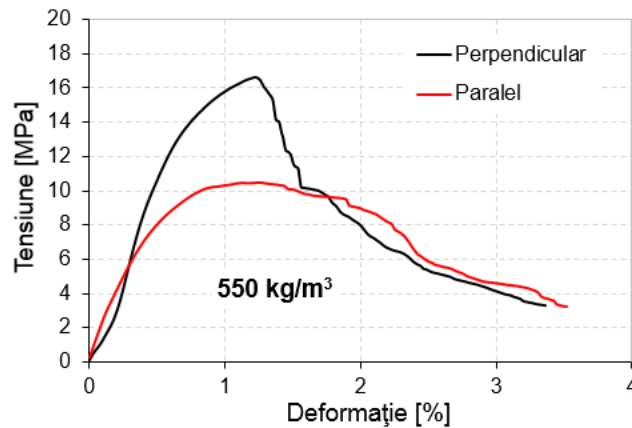


Fig. 26 Curbele tensiune-deformație la încovoiere in trei puncte. Influenta anizotropiei

Concluzii:

- Modulul de elasticitate si rezistenta la încovoiere sunt de aproximativ doua ori mai mari pe direcția de încărcare perpendiculara, comparativ cu direcția paralela (Figura 1).

## Polistirenul Expandat (EPS: EPS-50, EPS-80, EPS- 100, EPS- 120) – solicitare la încovoiere

Curbe caracteristice:

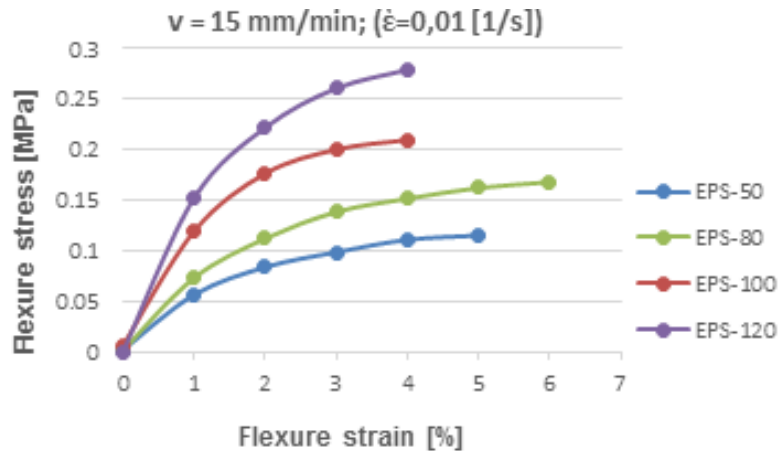


Fig. 27 Variatia rezistentei mecanice la solicitarea de incovoiere a polistirenului expandat (EPS), la  $v= 15\text{mm/min}$

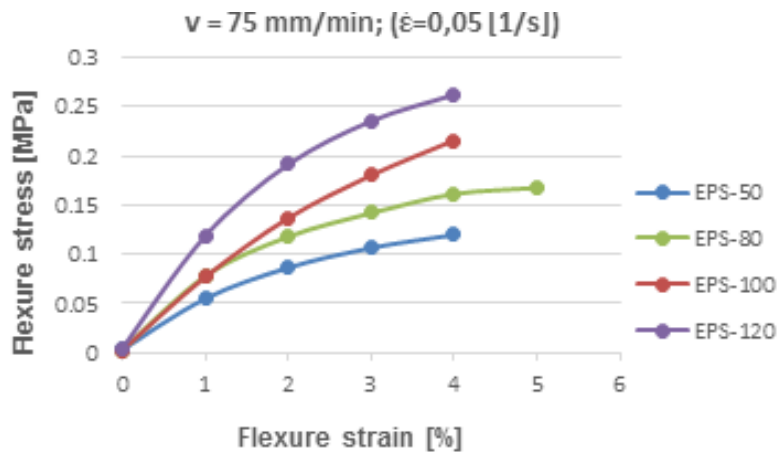


Fig. 28 Variația rezistenței mecanice la solicitarea de încovoiere a polistirenului expandat (EPS), la  $v=75\text{mm/min}$

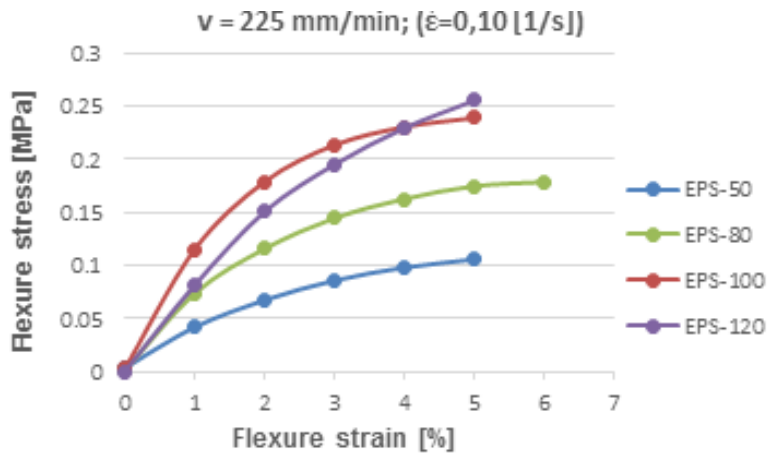


Fig. 29 Variația rezistenței mecanice la solicitarea de încovoiere a polistirenului expandat (EPS), la  $v=225\text{mm/min}$

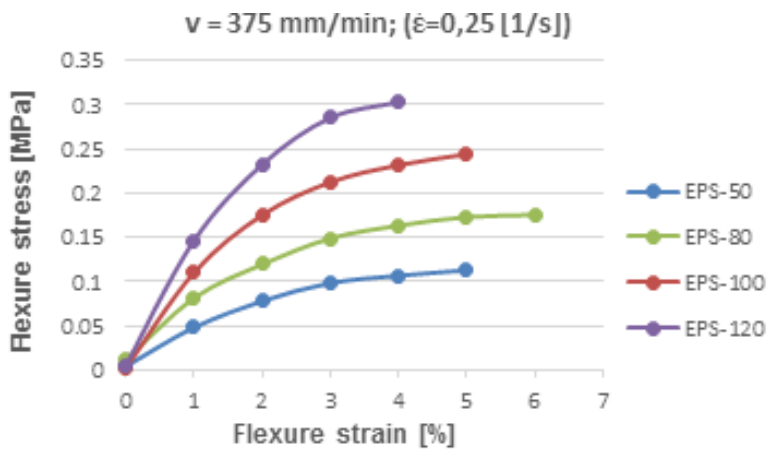


Fig. 30 Variația rezistenței mecanice la solicitarea de încovoiere a polistirenului expandat (EPS), la  $v=375\text{mm/min}$

**Tabelul 5.** Rezistența la încovoiere pentru tipurile de polistiren investigate la diverse viteze încercare

$\sigma$ [kPa]				$v$ [mm/min]	$\dot{\epsilon}$ [1/s]
EPS-50	EPS-80	EPS-100	EPS-120		
115,17	168,02	209,93	279,29	15	0,01
119,69	167,50	215,65	262,05	75	0,05
105,93	178,81	239,25	255,55	225	0,10
112,85	175,56	244,34	303,32	375	0,25

Concluzii:

- În timpul testelor de încovoiere a polistirenului expandat, s-a observat o influență a vitezei de încercare asupra rezistenței mecanice a acestuia.

## Bibliografie

N. Szolt, A. Máthé, I. Moldovan, B. Zakariás Comparații privind performanțele structurale ale panourilor sandwich din piața românească, Conference: Construieste cu STEEL A 14-A CONFERINTA NATIONALA DE CONSTRUCTII METALICEA, 2015: Cluj Napoca, Volume: ISBN 978-973-713-334-2

Catalog Tehnic Joris Ide, <http://www.jorisode.ro/>

Catalog Tehnic Kingspan, <https://www.kingspan.com/group/regions/europe-northern-asia/romania>

Catalog General Isopan, <http://www.isopan.ro/download/cataloage>

Catalog Tehnic Topanel, <http://www.topanel.ro/documentatie.html>



Catalog Tehnic Marcegaglia, <http://www.marcegaglia.ro/>

J. Kovácik, L. Marsavina, E. Linul, Poisson's Ratio of Closed-Cell Aluminium Foams, Materials, 11, 1904, 2018.

L Marșavina, O. Pop, R. Pepelan, Mark tracking technique for experimental determination of fracture parameters, Structural Integrity Procedia, 13, 1867-1872, 2018.

Article

# Poisson's Ratio of Closed-Cell Aluminium Foams

Jaroslav Kováčik <sup>1,\*</sup> , Liviu Marsavina <sup>2</sup> and Emanoil Linul <sup>2</sup> 

<sup>1</sup> Institute of Materials and Machine Mechanics, Slovak Academy of Sciences, Dúbravskácesta 9, 845 13 Bratislava, Slovak Republic

<sup>2</sup> Department of Mechanics and Strength of Materials, Politehnica University of Timisoara, 1 Mihai Viteazu Avenue, 300 222 Timisoara, Romania; liviu.marsavina@upt.ro (L.M.); emanoil.linul@upt.ro (E.L.)

\* Correspondence: ummsjk@savba.sk

Received: 10 August 2018; Accepted: 3 October 2018; Published: 7 October 2018



**Abstract:** A nondestructive impulse excitation technique was used to investigate Poisson's ratio of powder metallurgical pure closed-cell aluminium foams according to ASTM E 1876 within the foam density range of 0.430–1.390 g·cm<sup>-3</sup>. Instead of a constant value of 0.34, as according to Gibson and Ashby's assumption for the Poisson's ratio of metallic foams, the decrease of the Poisson's ratio with decreasing foam density was observed. Observed Poisson's ratio data were in the range of 0.21–0.34. To check the validity of the results, the Young's modulus was calculated using Poisson's ratio and its dependence on relative density was successfully modelled using the usual power law function with characteristic exponent of  $1.72 \pm 0.1$ . This confirms that the obtained experimental results for Poisson's ratio are valid. Finally, rule of mixture and percolation theory were used to model the observed decrease of Poisson's ratio with increasing porosity.

**Keywords:** aluminium foam; closed-cell foam; Poisson's ratio; porosity; nondestructive testing; modulus of elasticity

## 1. Introduction

When a material is compressed in one direction, it usually tends to expand in the other two directions perpendicular to the direction of the compression. This phenomenon is called the Poisson effect. Poisson's ratio  $\nu$  is a measure of this effect. Conversely, if the material is stretched rather than compressed, it usually tends to contract in the directions transverse to the direction of stretching. Again, the Poisson's ratio will be the ratio of relative contraction to relative expansion and will have the same value as above. The Poisson's ratio of a stable, isotropic, and linear elastic material cannot be less than  $-1.0$  not greater than  $0.5$  due to the requirement that Young's modulus, the shear modulus, and bulk modulus have positive values. Most materials have Poisson's ratio values ranging between  $0$  and  $0.5$ . In certain rare cases, a material (called auxetic) will actually shrink in the transverse direction when compressed (or expand when stretched), which will yield a negative value of the Poisson's ratio [1].

Aluminium foams, due to their metallic character and lightweight properties, have attracted interest from the science and technology communities since 1990 [2,3]. Obviously, their origin goes back to the beginning of the 20th century [4], and they were periodically reinvented and forgotten until 1990 [5–10]. Many articles, books, and conference proceedings have been published since 1990 in this field, mostly focusing on mechanical properties [11–17], and some of them also on thermal and electrical conductivities [18,19]. There is only one exception: there is no published paper regarding the experimental measurement of Poisson's ratio dependence on density.

There are several reasons for this. Basically, in industrial applications where foams are used (usually, as impact energy absorbers [12]), this value is not so important. Therefore, for FEM (Finite Element Method) calculations, the Poisson's ratio is often considered to be equal to the bulk aluminium Poisson's ratio. On the other hand, in the case of aluminium foams, it is not a simple task to measure

this value experimentally due to the cellular structure. Moreover, thanks to early plastic/brittle deformations of foams, even at small loads for such highly porous materials, it may also be that the continuum assumption is not reasonable.

It is generally assumed (according to Gibson and Ashby [20]) that the Poisson's ratio of aluminium foams is independent on porosity and the value is equal to the Poisson's ratio of used aluminium alloy 0.31–0.34 [20,21]. On the other hand, for modelling purposes in the plastic region, it is usually assumed that plastic Poisson's ratio of aluminium foams is zero [20]. This situation is usually found also outside aluminium foams. Scientists from many different fields in the finite-element simulation of porous materials or ceramic during FEM calculations in the elastic or ductile regimes usually assume that  $\nu$  is fixed at  $\sim 0.3$ . [22]. However, the latest findings in the research of nanoporous gold are contradict this: Poisson's ratio values of nanoporous gold around 0.18 have been observed. These are significantly lower than Poisson's ratio of pure gold (0.42) [23]. The experimental results in this field also indicate that the plastic Poisson's ratio of the investigated nanoporous gold is nonzero. Therefore, it is another reason to experimentally measure Poisson's ratio of aluminium foams.

Due to effects of clamping and plastic deformation of very thin cell walls at low stress levels, it is not easy to obtain the elastic properties of aluminium foam from tensile/compressive tests. Usually, it is done by performing a loading–unloading cycle during testing; however, there is already a certain level of plastic deformation even at early stages of stress that affects the results. Instead of tensile/compression tests or indentation tests, it is more appropriate to use nondestructive testing methods. One possibility is to use free vibrations of specimens of a given geometry. This vibration technique has been used for the determination of Young's modulus of aluminium foams since 1990s [3]. However, this requires long rods with a length much larger than the diameter of the rod. In this case, the modulus is proportional to the density and squared resonant frequency. Sadly, the determination of shear modulus is very sensitive to the heterogeneity inside the foam. Therefore, it is not possible to use this technique for Poisson's ratio measurement. The impulse excitation technique (IET) [24] is a nondestructive material characterization technique used to find the elastic properties and internal friction of a material of interest. It measures the resonant frequencies to calculate the Young's modulus, shear modulus, Poisson's ratio, and internal friction of disc-shaped samples. The measurement principle is based on tapping the sample with a small projectile and recording the induced vibration signal with a microphone or laser vibrometer. Afterwards, the acquired vibration signal in the time domain is converted to the frequency domain by a fast Fourier transformation. Dedicated software can determine the resonant frequency with high accuracy to calculate the elastic properties based on the classical beam theory. The advantage of this method is that it is applicable to porous and brittle materials due to small strains. Therefore, it was expected that the new vibration techniques would enable us to measure Poisson's ratio of aluminium foams directly. The aim of the present work was to use the IET to measure the Poisson's ratio of pure aluminium foam and to confirm its independence on porosity.

## 2. Experimental

Aluminium foam samples were prepared via a powder metallurgical route from aluminium alloy powder Al 99.7 (Fe 0.13 wt. %, Si 0.10 wt. %, Al balanced, Mepura GmbH (Ranshofen, Austria), powder size 63–400  $\mu\text{m}$ ) that was mixed together with a foaming agent (0.7 wt. % of  $\text{TiH}_2$ , Chemetall GmbH, Frankfurt am Main, Germany, Grade N, grain size below 60  $\mu\text{m}$ , powder size  $d_{50} = 14.52 \mu\text{m}$ ) cold isostatic pressed and then continuously hot extruded at 500  $^\circ\text{C}$  into a foamable precursor. The various quantities of precursor were foamed up in a steel mold at 800  $^\circ\text{C}$  for different times to obtain different foam densities. The prepared foams were flat plates with the dimensions of 140  $\times$  140  $\times$  8.3/9.61  $\text{mm}^3$  (Figure 1a). The foamed plates' densities were in the range of 0.430–1.550  $\text{g}\cdot\text{cm}^{-3}$ . Particularly, foams with higher densities were prepared by interrupting the foaming process at early stages of gas evolution from the foaming agent and were more anisotropic as low-density foams.

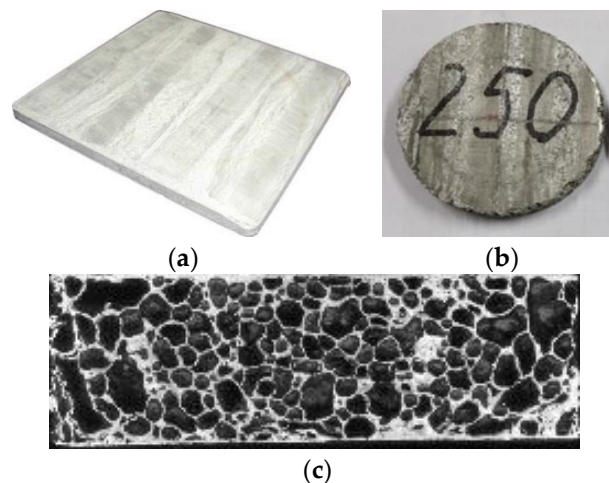


**Figure 1.** (a) Prepared aluminium foam plate, (b) disc sample for the impulse excitation technique (IET) test, and (c) typical cell structure of foam, density  $0.50 \text{ g}\cdot\text{cm}^{-3}$ .

The samples for the determination of Poisson's ratio of aluminium foams were cut using a milling machine from foam plates. The typical geometry of the samples was around disc of  $\varphi 60 \text{ mm} \times 8.3/9.61 \text{ mm}$  (see Figure 1b). A foam disc with a density of  $1.550 \text{ g}\cdot\text{cm}^{-3}$  was not suitable for the determination of its Poisson's ratio as its resonant frequency ratio  $f_1/f_2$  (see below for definition) was outside of the range required by the used measurement method. However, this result indicated that the used measurement method was precise enough to detect heterogeneous and anisotropic samples. Therefore, only the density range of  $0.430\text{--}1.390 \text{ g}\cdot\text{cm}^{-3}$  for round discs was further used for the results and discussion.

An IET was used to measure Poisson's ratio using a Resonant Frequency & Damping Analyser (IMCE, Genk, Belgium). To determine the Poisson's ratio of aluminium foams, vibrational tests were carried out on round disc samples according to ASTM E 1876 [24]. From the ratio between the flexural and the antilexural frequency (see Figure 2), it is possible to calculate the Poisson's ratio using a numerical solution by Martincek [25] and Glandus [26].

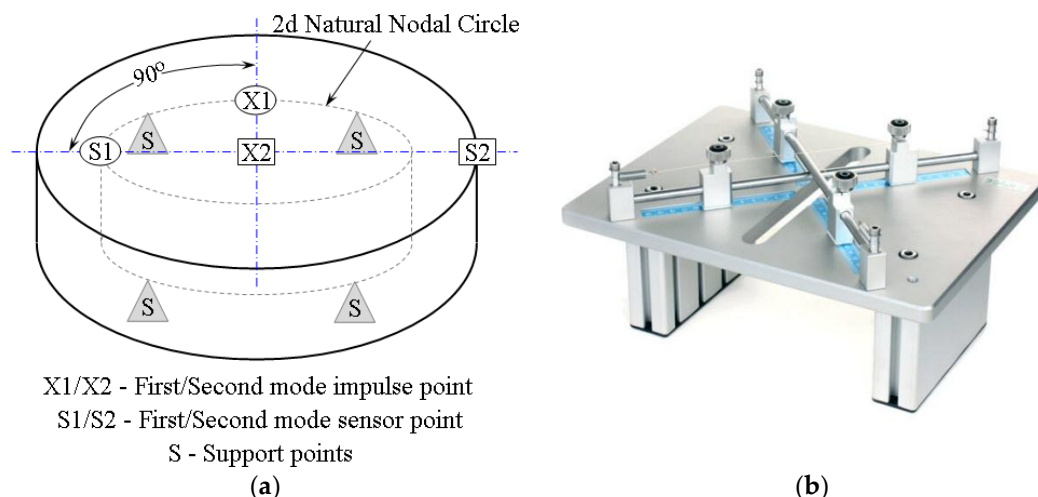


**Figure 2.** (a) Support, impulse, and sensor points for first and second natural vibrations in discs according to ASTM E 1876. (b) Picture of used precision wire support for foam disc samples.

Basically, the Poisson's ratio is determined using the resonant frequencies of the first two natural vibration modes. The dynamic Young's modulus and dynamic shear modulus are then calculated using the Poisson's ratio, the experimentally determined fundamental resonant frequencies, and the

specimen dimensions and mass. The first natural vibration occurs when the displacements in the cross-sectional plane (the plane that is parallel to the flat of the disc) are normal to the plane and symmetrical around two orthogonal diameters in the plane of the disc, producing a twisting of the disc. This is an orthogonal antilexural mode of vibration. For the first natural vibration mode, the nodes are located along two orthogonal diameters, offset 45° from the point where the vibration was induced. The antinodes are located along two orthogonal (90° offset) diameters in the disc, with one diameter intersecting the point where the vibration was induced.

The second natural vibration occurs when the displacements in the cross-sectional plane (the plane that is parallel to the flat of the disc) are normal to the plane and are uniform in displacement for a given radial distance from the centre point through the entire 360° arc. This is axisymmetric flexural vibration. For the second natural vibration mode of a disc, the nodes are located in a circle concentric with the centre of the disc with a fractional radius of 0.681 of the disc radius. The antinodes are located at the centre and around the circumference of the disc specimen.

The derivation and use of the equations for calculating the Poisson's ratio and moduli from disc-shaped specimens are described in detail in References [25,26]. Martinec [25] gives the derivation and procedures for the baseline calculation. The fundamental equation defining the relationship between the natural resonant frequency, the material properties, and the specimen dimensions is given by Martinec as:

$$f_i = \frac{K_i}{2\pi r^2} \sqrt{\frac{A}{\rho t}} \quad (1)$$

where  $f_i$  is the resonant frequency of interest,  $K_i$  is the geometric factor for that resonant frequency,  $r$  is the radius of the disc,  $A$  is the plate constant ( $A = Et^3/[12 \times (1 - \nu^2)]$ ),  $t$  is the disc thickness,  $\rho$  is the density of the disc,  $E$  is Young's modulus of elasticity, and  $\nu$  is the Poisson's ratio for the disc material. This is a general equation that is valid for both the first natural and second natural vibrations. Glandus [26] supplements the Martinec article with more extensive tables for the geometric factors  $K_i$  and for determining Poisson's ratio. The Poisson's ratio is determined directly from the experimental values for the first and second natural resonant frequencies given in tables in the above mentioned references [25,26] and as well in ASTM E 1876 [24]. There, the value for Poisson's ratio ( $\nu$ ) is interpolated from the table using the ratio of the second natural resonant frequency to the first natural resonant frequency ( $f_2/f_1$ ) correlated with the ratio of the specimen thickness to the specimen radius ( $t/r$ ). The following requirements must be met: the ratio of the flexural and antilexural resonant frequencies is in the range  $1.35 \leq f_1/f_2 \leq 1.90$ , and diameter  $D$  and thickness  $t$  of the specimen ought to be larger than the ratio  $D/t \geq 4$ .

For the Young's modulus of a disc, two calculations of  $E$  ( $E_1$  and  $E_2$ ) are made independently from the two resonant frequency measurements, and then a final value  $E$  is determined by averaging the two calculated values  $E_1$  and  $E_2$ :

$$E_1 = \left[ 12\pi f_1^2 D^2 m (1 - \nu^2) \right] / (K_1^2 t^3) \quad (2)$$

$$E_2 = \left[ 12\pi f_2^2 D^2 m (1 - \nu^2) \right] / (K_2^2 t^3) \quad (3)$$

where  $E$ ,  $E_1$ , and  $E_2$  is the average, first, and second calculation of Young's modulus, respectively. There,  $f_1$  is the first and  $f_2$  is the second natural resonant frequency of the disc,  $D$  is the diameter and  $m$  is the mass of the disc,  $\nu$  is Poisson's ratio for the specimen as determined previously,  $K_1$  is the first natural geometric factor from the table (function of  $t/r$  and  $\nu$ ) and  $K_2$  is the second natural geometric factor from the other table (again, function of  $t/r$  and  $\nu$ ),  $t$  is the thickness of the disc, and  $r$  is the radius of the disc.

To properly determinate the elastic properties of the disc specimens, it is necessary to fulfil conditions of the specimen geometry and the proper positioning of the support points below the sample and the impulse and sensor points above the sample (see Figure 2) [27]. According to ASTM,

the ratio between the diameter and the thickness of the specimen must be at least 4. For all investigated foam samples, this ratio was found to be in the range of 6–8. Then, a support nodal circle diameter was calculated as 0.681 for the specimen diameter of each disc, leading to the value of 40.86 mm. Finally, the sample was freely excited by a light impact strike with a special hammer at impulse points (X1 and X2 in Figure 2) and the resonant frequency was measured by a microphone placed in the sensor point for both the first and second excitation modes (S1 and S2 in Figure 2). To ensure repeatability, at least five readings of resonant frequency were done and the average value was used for the first and the second natural frequencies, respectively. Measured resonant frequencies for all samples had readings with a variation smaller than 1%, which agrees with ASTM E 1876. Finally, all flexural and antiflexural resonant frequencies were in the range of  $1.35 \leq f_1/f_2 \leq 1.90$  for all samples, except the abovementioned one for the densest sample. Finally, Poisson's ratio was determined directly from the measured resonant frequencies using the tabulated values of  $f_1/f_2$  and  $t/r$ . Then, the Young's modulus values were determined via Equations (2) and (3) using the corresponding ASTM tables.

### 3. Results and Discussion

The Poisson's ratio of pure aluminium and aluminium alloys is in the range of 0.31–0.34 [20]. In Gibson and Ashby's book, they put forward the opinion that the Poisson's ratio of aluminium foams is equal to the Poisson's ratio of the used matrix metal or metal alloy and is independent of density [21]. To avoid potential reactions and consequent phase creation inside of the foam cell walls, pure aluminium powder was used in this study for the foam preparation. Therefore, the foam cell walls' composition is quite simple. There are present aluminium, Ti localized inside of cell walls (0.7 wt. % from decomposed foaming agent), and finally, alumina (around 1 wt. % from powder envelopes, unfortunately not visible on SEM microscope) [11]. This means that there are no stabilizing additions such as 10–20 vol.% of  $Al_2O_3$ , SiC,  $TiB_2$ , etc. Therefore, it can be expected that the Poisson's ratio value of 0.34 will be observed within all the investigated porosity ranges.

Unfortunately, the Poisson's ratio of the pure aluminium foam measured using the impulse excitation nondestructive technique in the density range of 0.430–1.390  $g \cdot cm^{-3}$  showed a different result. The Poisson's ratio of closed-cell pure powder metallurgical PM aluminium foam is density dependent (see Table 1 and Figure 3). It was experimentally observed that with decreasing density, the Poisson's ratio of aluminium foams decreases from the value of 0.34 down to 0.21. This result is similar to the porosity dependence of Poisson's ratio observed previously in porous solids and ceramics [28,29].

**Table 1.** Measured Poisson's ratio and Young's modulus values of pure PM aluminium foams.

Density ( $g/cm^3$ )	Relative Density (-)	Porosity (-)	Poisson's Ratio (-)	E (GPa)
0.433	0.160	0.840	0.214	$4.93 \pm 0.12$
0.443	0.164	0.836	0.235	$5.13 \pm 0.07$
0.448	0.166	0.834	0.275	$5.03 \pm 0.22$
0.453	0.168	0.832	0.255	$5.20 \pm 0.07$
0.461	0.171	0.829	0.255	$5.17 \pm 0.05$
0.469	0.174	0.826	0.235	$5.49 \pm 0.12$
0.504	0.187	0.813	0.268	$5.45 \pm 0.18$
0.540	0.200	0.800	0.235	$6.65 \pm 0.03$
0.688	0.255	0.745	0.275	$6.68 \pm 0.18$
1.394	0.516	0.484	0.312	$16.47 \pm 0.18$
2.700	1.000	0.000	0.340	70



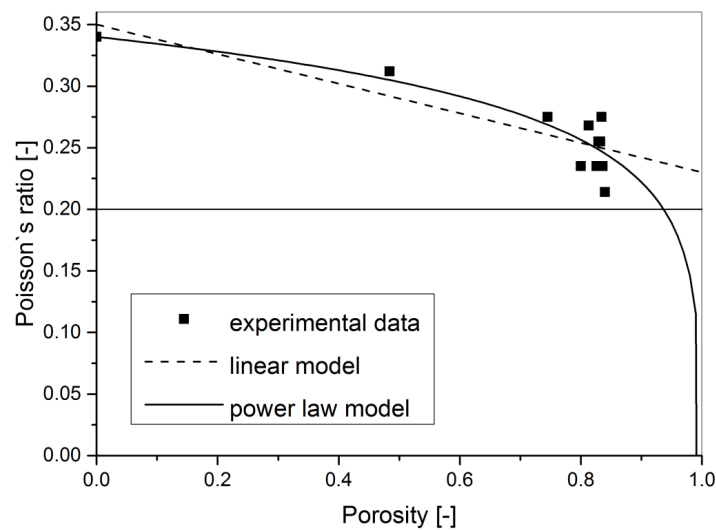


**Figure 3.** The porosity dependence of Poisson's ratio of pure aluminium foams. Plotted are the linear model, the power law model, and also the 0.2 constant.

The Young's modulus data according to Equations (2) and (3) were calculated to check the validity of the obtained Poisson's ratio results. Further, the Young's modulus dependence on porosity modelled using percolation [18] or Gibson and Ashby's power law model [20] was

$$E = E_0(1 - \phi)^{f_E} \quad (4)$$

where  $E$ ,  $E_0$  is foam modulus and modulus of bulk aluminium,  $\phi$  is the porosity, and  $f_E$  is the characteristic exponent for the power law dependence of Young's modulus. It is usually accepted that characteristic exponent of aluminium foams is in the range of 1.8–2.2 [20].

The fitting results for the density dependence of Young's modulus led to the characteristic exponent of  $f_E = 1.72 \pm 0.10$  with  $R^2 = 0.982$  (Figure 4). The observed value mostly coincided with the experimental results for various types of aluminium foams between 1.8 and 2.2 [20]. The lower value of the characteristic exponent is probably due to the certain anisotropy of the foam samples.

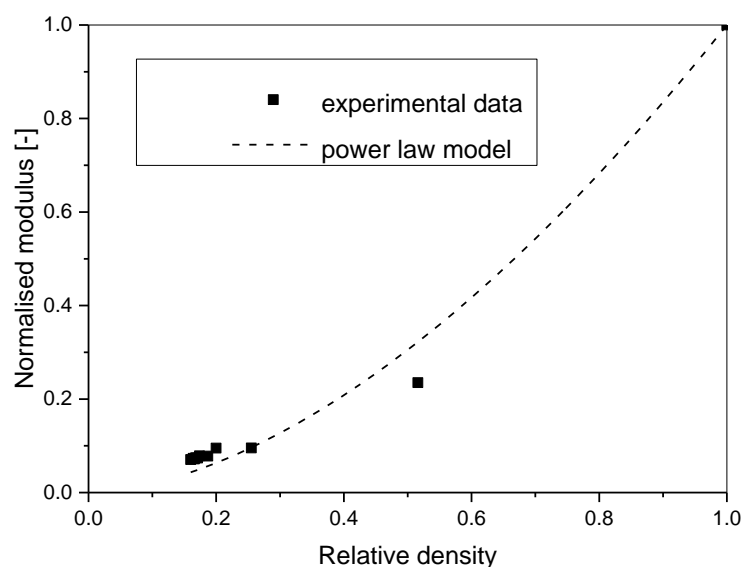


**Figure 4.** The dependence of the normalised Young's modulus of pure aluminium foams on relative density. Plotted line is the power law model with  $R^2 = 0.982$ ,  $f_E = 1.72 \pm 0.10$ .

It can be concluded that the obtained Young's modulus experimental results and the validity of the power law model for Young's modulus porosity dependence proved that the observed Poisson's ratio decrease with increasing porosity was correctly measured.

Therefore, the originally accepted hypothesis that the Poisson's ratio of aluminium foams is constant at all density ranges and has a value of 0.34 was proved to be incorrect in the case of closed-cell pure aluminium PM-prepared foams. It implies that the hypothesis can be also incorrect for other types of aluminium and metallic foams.

The elastic Poisson's ratio of open-cell AlSi0.5Mg aluminium foams was investigated numerically by Wicklein and Thoma [30]. Finite-element discretization, which has been derived from real foam specimens by computer tomography data, was used. They found that Poisson's ratio is approximately constant, with an average value of 0.23 in the relative density range of 0.35–0.5. The Poisson's ratio value for open-cell AlSi0.5Mg foams is smaller than the Poisson's ratio value for the AlSi0.5Mg alloy, thus supporting the experimentally observed dependence of Poisson's ratio on porosity in the present paper.

Due to the chosen matrix composition (pure Al with 0.7 wt. % Ti), we can exclude potential phase creations inside foam cell walls affecting the mechanical properties of the investigated foams. For this reason, only the porosity and heterogeneity of the foam structure can affect the Poisson's ratio values of the investigated foams. From Figure 1c, it is clear that some scatter of experimental data for low-density foams (with 80–84% porosity) took place. The reason for this can be the increase of pore size with decreasing density.

It is usually expected for metallic foams that the geometry of the sample contains in all directions at least 10 pores to avoid certain heterogeneity effects. In our case, the average pore size is around 0.8–1 mm at the density of  $0.50 \text{ g}\cdot\text{cm}^{-3}$ . This means that the local variations of porosity affect the measured values for 80–84% porosity, thus leading to the large scatter of experimental data. With increasing density, the pore size decreases, thus diminishing this effect [11].

When the pure aluminium Poisson's ratio of 0.34 was used in the data-set, there were three points outside the clustered data points for 80–84% porosity. Even when only data for 0%, 48%, and 75% porosity were used, the observed decrease of Poisson's ratio was obvious due to the higher homogeneity of the foam structure for these points.

It can be concluded that the higher the foam porosity, the higher the scatter of the measured data. This is due to the fact that all IET methods based on vibrations need 2D samples due to the beam theory calculation with the third dimension being as small as possible. Therefore, certain error will always be there in the case of metallic foams.

In principle, it is possible to calculate the porosity dependence of Poisson's ratio from two elastic moduli, e.g., shear ( $G$ ) and longitudinal Young moduli ( $E$ ):

$$\nu = \frac{E}{2G} - 1 \quad (5)$$

While there are many models that can predict the porosity dependence of elastic and shear modulus, models to predict Poisson's ratio  $\nu$  are mostly developed from Equation (5), and many of them are very complex. As the observed experimental results for Poisson's ratio had high data scatter, the focus was on models and explanations that were as simple as possible.

Most models created for porous solids which are based on Equation(5) lead to the conclusion that with increasing porosity, there is a tendency for the Poisson's ratio of porous ceramic to approach the constant value [28,29] of 0.2, as this value seems to be an "attractor" for the effective Poisson's ratio. However, when the Poisson's ratio of the solid phase  $\nu_0$  is below 0.2 ( $\nu_0 < 0.2$ ), the effective Poisson's ratio tends to increase with increasing porosity to this value.

A similar attracting behaviour was proposed originally by Kitazono et al. [31] for metallic foams using a continuum micromechanical model (with the equivalent inclusion method and the mean-field approximation). They stated that Poisson's ratio of foam decreases with the decrease of the relative

density if Poisson's ratio of matrix metal  $>0.2$  and increases if Poisson's ratio of matrix metal  $<0.2$  in the certain parameter limit ( $p = 0$ ). Only when Poisson's ratio of matrix metal  $=0.2$  does Poisson's ratio of foam become independent of the relative density. Since the Poisson's ratio of most metals and alloys is more than 0.2, the micromechanical model predicts that the Poisson's ratio of metal foams monotonously decreases with the decreasing of the relative density and approaches a constant value of 0.25 [31]. Observed values in the present paper at low porosity show that the Poisson's ratio of the investigated foams deviates from this attractor value of 0.25, as lower values of Poisson's ratio down to 0.21 were measured.

In another approach, the Poisson's ratio can be in the simplest way modelled by a linear approximation [29]:

$$\nu = \nu_0 + b \times \phi = \nu_0 + \frac{3(1 - 5\nu_0)(1 - \nu_0^2)}{2(7 - 5\nu_0)} \times \phi \quad (6)$$

where  $\nu$  is the effective Poisson's ratio,  $\nu_0$  is the Poisson's ratio of the corresponding bulk material, and  $\phi$  is the porosity. However, this approach has the typical shortcomings of mixture-based theories. In the case of porous ceramics (ceramic composites where one phase consists of air-filled voids exhibiting zero Poisson's ratio), the rule of mixture for the effective Poisson's ratio evidently fails, since the effective Poisson's ratio did not approach the zero value (as should be the case for the rule of mixture) [22].

After fitting the observed Poisson's ratio results to this linear approximation model, it was clear that it described them well (see Figure 3). The only drawback was that the calculated constant  $b$  for the bulk aluminium Poisson's ratio value of 0.34 and fitted values of constant  $b = (1 - 5\nu_0) \cdot (1 - \nu_0^2) / (2 \times (7 - 5\nu_0))$  were  $-0.175$  and  $-0.12 \pm 0.02$  (see Table 2), respectively. This was a difference of about 31% for constant  $b$ .

**Table 2.** Fitting results for the experimental data for the linear model and the power law model with R squared (coefficient of determination).

Model	Equation	$\nu_0$ Model	$\nu_0$ Fit Result	$b$ Theoretical	Fit Result	$R^2$
Linear	$\nu = \nu_{0+} + b \times \phi$	0.34	$0.35 \pm 0.02$	$-0.175$	$b = -0.12 \pm 0.02$	0.698
Power law	$\nu = (\nu_0 + 1)(1 - \phi)^{f_\nu} - 1$	0.34	$0.34 \pm 0.02$	-	$f_\nu = 0.04 \pm 0.01$	0.761

Another possibility is to use percolation theory, which works with a threshold idea that is based on the formation of long-range connectivity in random systems. Below the threshold, a giant connected component does not exist, while above it, there is a giant component of the order of the system size [32,33]. For metallic foam, the percolation threshold is the porosity at which the mechanical properties of the porous material become zero (because the foam does not exist anymore as an entity in the order of the system size).

Therefore, the Poisson's ratio of solids was modelled using the power law dependence on porosity on the basis of the percolation theory [33] by incorporating the percolation threshold into the model [34–37]. This leads to the well-known percolation power-law relation or differential approximation [34,38]. As was mentioned above, the percolation threshold is the porosity at which the mechanical properties of a porous material become zero. Garboczi et al. [39] showed that for the special case of overlapping ellipsoids, a percolation threshold above 99.9 vol.% can be observed. Based on this assumption, the percolation equation for the investigated aluminium foams followed a simplified form [34]:

$$\nu = (\nu_0 + 1)(1 - \phi)^{f_\nu} - 1 \quad (7)$$

where  $f_\nu$  is characteristic exponent for Poisson's ratio.

The observed experimental data were then fitted to Equation (7) and the obtained fitting results are also plotted in Figure 3 and are listed in Table 2. The  $R^2$  value for this model is almost the same as the  $R^2$  value of the linear approximation. Basically, both models can be used to predict the observed Poisson's ratio dependence on porosity within the investigated porosity range. The only difference is

that the Poisson's ratio dependence based on the percolation model tends to the zero value for porosity approaching 100%.

Summarising, the decrease of Poisson's ratio dependence on porosity was observed experimentally for closed-cell pure PM aluminium foams. Poisson's ratio values were in the range of 0.21–0.34. Both the linear approximation and percolation models are suitable to describe the observed decrease within the investigated porosity range.

#### 4. Conclusions

Direct measurement of the Poisson's ratio of PM pure aluminium foam was performed in the density range of 0.430–1.390 g·cm<sup>-3</sup> via using an impulse excitation technique according to ASTM E 1876. The decrease of Poisson's ratio with decreasing density of aluminium foams was observed in the range of 0.34–0.21. This contradicts Gibson and Ashby's assumption that the Poisson's ratio of aluminium foams is constant at all density ranges and has the Poisson's ratio value of pure aluminium (0.34).

The percolation model or Gibson and Ashby's model was used to describe the modulus of elasticity dependence on relative density. The results for Young's modulus confirmed the validity of Poisson's ratio measurement as the results for the modulus coincide with previous results observed for the modulus of other aluminium foams. The observed characteristic exponent was  $1.72 \pm 0.1$ .

The rule of mixture and the derived percolation model were used to explain the observed behaviour of Poisson's ratio with porosity. It was shown that both the linear approximation and percolation models are suitable to describe the observed decrease. To determine which model is better, it will be necessary to measure higher-porosity foams, which will be the aim of future work.

**Author Contributions:** Resources, Writing–Review & Editing, J.K.; Funding Acquisition, Supervision, L.M.; Investigation, E.L.

**Funding:** This research was funded by the grant of the Romanian Ministry of Research and Innovation, CCCDI – UEFISCDI, project number PN-III-P1-1.2-PCCDI-2017-0391 / CIA\_CLIM—Smart buildings adaptable to the climate change effects, within PNCDI III, Slovak Research and Development Agency under bilateral agreement between UPT and SAS, contract no. SK-RO-0014-12 and 653/2013, Slovak Research and Development Agency grants APVV-0692-12, APVV-17-0580 and Slovak Grant Agency (VEGA grants 2/0152/17 and 2/0044/17).

**Acknowledgments:** The authors are grateful to Tudor Voiconi for his experimental work.

**Conflicts of Interest:** The authors declare no conflict of interest.

#### References

1. Novak, N.; Vesenjaj, M.; Ren, Z. Auxetic Cellular Materials—a Review. *J. Mech. Eng.* **2016**, *62*, 485–493. [[CrossRef](#)]
2. Kunze, H.D.; Baumeister, J.; Banhart, J.; Weber, M. PM Technology for the Production of Metal Foams. *Powder Met. Int.* **1993**, *25*, 182–185.
3. Simančík, F.; Jerz, J.; Kováčik, J.; Minár, P. Aluminium foam—A new light-weight structural material. *Kovove Mater.* **1997**, *35*, 265–277.
4. De Meller, M.A. Produit Metallique pour L'Obtention D'Objets Lamines, Moulesouautres, et Procedes pour sa Fabrication. French Patent 615,147, 1926.
5. Sosnick, B. Process of Making Foamlike Mass of Metal. U.S. Patent 2,434,775, 1948.
6. Elliott, J.C. Method of Producing Metal Foam. U.S. Patent 2,751,289, 1956.
7. Allen, B.C.; Mote, M.W.; Sabroff, A.M. Method of Making Foamed Metal. U.S. Patent 3,087,807, 1963.
8. Berry, C.B. Foamed Metal. U.S. Patent 3,671,221, 1972.
9. Niebylski, L.M.; Fanning, R.J. Metal foams as energy absorbers for automobile bumpers. *Soc. Automot. Eng. Inc.* **1972**, *1676*, 720490. [[CrossRef](#)]
10. Thornton, P.H.; Magee, C.L. The deformation of aluminium foams. *Metall. Trans. A.* **1975**, *6A*, 1253. [[CrossRef](#)]
11. Banhart, J. Manufacture, characterisation and application of cellular metals and metal foams. *Prog. Mater. Sci.* **2001**, *46*, 559–632. [[CrossRef](#)]

12. García-Moreno, F. Commercial Applications of Metal Foams: Their Properties and Production. *Materials* **2016**, *9*, 85. [[CrossRef](#)] [[PubMed](#)]
13. Marsavina, L.; Kováčik, J.; Linul, E. Experimental validation of micromechanical models for brittle aluminium alloy foam. *Theor. Appl. Fract. Mech.* **2016**, *83*, 11–18. [[CrossRef](#)]
14. Kováčik, J.; Simančík, F. Comparison of zinc and aluminium foam behavior. *Kovove Mater.* **2004**, *42*, 79–90.
15. Voiconi, T.; Linul, E.; Marsavina, L.; Kováčik, J.; Kneć, M. Experimental determination of mechanical properties of aluminium foams using Digital Image Correlation. *Key Eng. Mat.* **2014**, *601*, 254–257.
16. Linul, E.; Serban, D.A.; Marsavina, L.; Kováčik, J. Low-cycle fatigue behaviour of ductile closed-cell aluminium alloy foams. *Fatigue Fract. Eng. Mater. Struct.* **2017**, *40*, 597–604. [[CrossRef](#)]
17. Linul, E.; Movahedi, N.; Marsavina, L. On the Lateral Compressive Behavior of Empty and Ex-Situ Aluminum Foam-Filled Tubes at High Temperature. *Materials* **2018**, *11*, 554. [[CrossRef](#)] [[PubMed](#)]
18. Kováčik, J.; Simančík, F. Aluminium Foam—Modulus of Elasticity and Electrical Conductivity according to Percolation Theory. *Scr. Mater.* **1998**, *39*, 239–246.
19. Solórzano, E.; Reglero, J.A.; Rodríguez-Pérez, M.A.; Lehmhus, D.; Wichmann, M.; De Saja, J.A. An experimental study on the thermal conductivity of aluminium foams by using the transient plane source method. *Inter. J. Heat Mass Transf.* **2008**, *51*, 6259–6267. [[CrossRef](#)]
20. Ashby, M.F.; Evans, A.G.; Fleck, N.A.; Gibson, L.J.; Hutchinson, J.W.; Wadley, H.N.G. *Metal Foams: A Design Guide*; Butterworth-Heinemann: Boston, MA, USA, 2000; p. 43.
21. Gibson, L.J.; Ashby, M.F. *Cellular Solids: Structure and Properties*, 2nd ed.; Cambridge University Press: Cambridge, UK, 1997.
22. Greaves, G.N.; Greer, A.L.; Lakes, R.S.; Rouxel, T. Poisson's ratio and modern materials. *Nat. Mater.* **2011**, *10*, 823–837. [[CrossRef](#)] [[PubMed](#)]
23. Mangipudi, K.R.; Epler, E.; Volkert, C.A. On the multiaxial yielding and hardness to yield stress relation of nanoporous gold. *Scr. Mater.* **2018**, *146*, 150–153. [[CrossRef](#)]
24. *Standard Test Method for Dynamic Young's Modulus, Shear Modulus, and Poisson's Ratio by Impulse Excitation of Vibration*; ASTM E1876; ASTM International: West Conshohocken, PA, USA, 2015.
25. Martinček, G. The determination of poisson's ratio and the dynamic modulus of elasticity from the frequencies of natural vibration in thick circular plates. *J. Sound Vib.* **1965**, *2*, 116–127. [[CrossRef](#)]
26. Glandus, J.C. Rupture Fragile et Résistance Aux Chocthermiques de Céramiques a Usages Mécaniques. Ph.D. Thesis, University of Limoges, Limoges, France, 1981.
27. Voiconi, T. Mechanical Characterisation of Metallic of Foams and Structures Containing Metallic Foams. Ph.D. Thesis, Politehnica University of Timisoara, Timisoara, Romania, 2015.
28. Pabst, W.; Gregorová, E. Effective elastic properties of alumina-zirconia composite ceramics—Part II: Micromechanical modeling. *Ceram. Silik.* **2004**, *48*, 14–23.
29. Gregorová, E.; Pabst, W.; Uhlířová, T.; Nečina, V.; Veselý, M.; Sedlářová, I. Processing, microstructure and elastic properties of mullite-based ceramic foams prepared by direct foaming with wheat flour. *J. Eur. Ceram. Soc.* **2016**, *36*, 109–120. [[CrossRef](#)]
30. Wicklein, M.; Thoma, K. Numerical investigations of the elastic and plastic behavior of an open-cell aluminium foam. *Mater. Sci. Eng. A* **2005**, *397*, 391–399. [[CrossRef](#)]
31. Kitazono, K.; Sato, E.; Kuribayashi, K. Application of mean-field approximation to elastic-plastic behavior for closed-cell metal foams. *Acta Mater.* **2003**, *51*, 4823–4836. [[CrossRef](#)]
32. Torquato, S. *Random Heterogeneous Materials—Microstructure and Macroscopic Properties*; Springer: New York, NY, USA; pp. 303–646.
33. Stauffer, D.; Aharony, A. *Introduction to Percolation Theory*, 2nd ed.; Taylor & Francis: London, UK, 1992.
34. Kováčik, J. Correlation between Poisson's ratio and porosity in porous materials. *J. Mater. Sci.* **2005**, *41*, 1247. [[CrossRef](#)]
35. Pal, R. Porosity-dependence of Effective Mechanical Properties of Pore-solid Composite Materials. *J. Compos. Mater.* **2005**, *39*, 1147. [[CrossRef](#)]
36. Kováčik, J.; Jerz, J.; Mináriková, N.; Marsavina, L.; Linul, E. Scaling of compression strength in disordered solids: Metallic foams. *Frattura Integr. Strutturale* **2016**, *36*, 55–62. [[CrossRef](#)]
37. Kováčik, J.; Orovčík, L.; Jerz, J. High-temperature compression of closed cell aluminium foams. *Kovove Mater.* **2016**, *54*, 429–440.

38. Sevostianov, I.; Kachanov, M. Connections between elastic and conductive properties of heterogeneous materials. *Adv. Appl. Mech.* **2009**, *42*, 69–252. [[CrossRef](#)]
39. Garboczi, E.J.; Snyder, K.A.; Douglas, J.F. Geometrical percolation threshold of overlapping ellipsoids. *Phys. Rev. E* **1995**, *52*, 819–827. [[CrossRef](#)]



© 2018 by the authors. Licensee MDPI, Basel, Switzerland. This article is an open access article distributed under the terms and conditions of the Creative Commons Attribution (CC BY) license (<http://creativecommons.org/licenses/by/4.0/>).



ECF22 - Loading and Environmental effects on Structural Integrity

# Mark tracking technique for experimental determination of fracture parameters

Liviu Marşavina<sup>a,\*</sup>, Octavian Pop<sup>b</sup>, Raluca Pepelan<sup>a</sup>

<sup>a</sup> University Politehnica Timisoara, Department Mechanics and Strength of Materials, Timisoara 300222 Romania

<sup>b</sup> Universite de Limoges, GC2D, EA 3178, Egletons F-19300, France

## Abstract

The Mark Tracking method represents a modern and simple optical method to determine the displacement and strain fields. The principle of the marks tracking method is based on the comparison between two images acquired before and after sample deformation. The algorithm of method track the local displacement of the marks in two directions. Having measured displacements in certain points around the crack it is relative simple to estimate the Stress Intensity Factor (SIF) by displacement correlation methods. The students can compare different data processing algorithms for extracting the SIF's. Basically, a simple geometry like Single Edge Notch Bend specimen loaded in Three Point Bending was tested, for which the exact solution of SIF is well known. The reliability of experimental technique is assessed by comparing the results with the exact solution.

© 2018 The Authors. Published by Elsevier B.V.  
Peer-review under responsibility of the ECF22 organizers.

*Keywords:* mark tracking, displacement correlation, stress intensity factor

## 1. Introduction

Fracture parameters like Stress Intensity Factors (SIF), Energy Release Rate (ERR), J-Integrals (J) and Crack Tip Opening Displacement (CTOD) are basic parameters in structural integrity assessment based on Fracture Mechanics concept, Saouma (2007). For linear elastic materials the fracture criterion based on Stress Intensity Factor  $K$  and fracture toughness  $K_{IC}$  is the common used:  $K < K_{IC}$ . In order to apply this criteria two sets of data are required: the value of  $K$  which characterize the stress singularity at the crack tip and depends on applied load, crack length, geometry of cracked body and loading type. Values of SIF's could be determined analytically, numerically or experimentally, Fig. 1.

\* Corresponding author.  
E-mail address: [liviu.marsavina@upt.ro](mailto:liviu.marsavina@upt.ro)

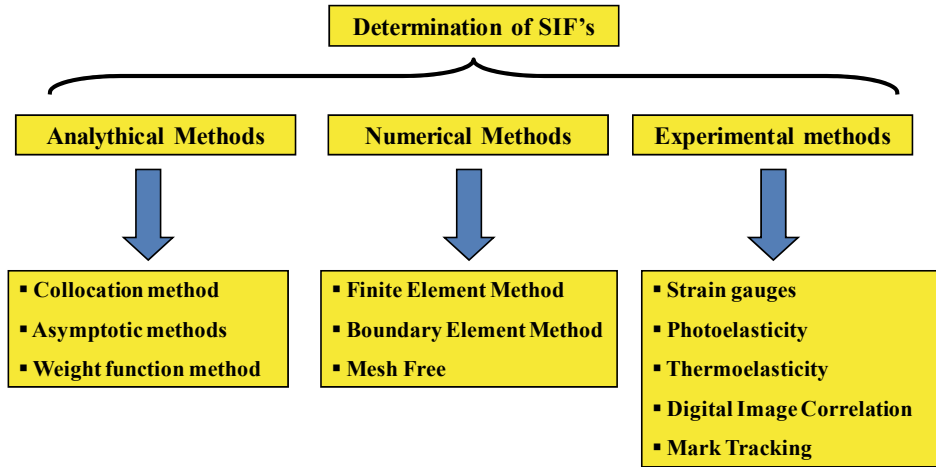


Fig.1 Stress Intensity Factors determination methods

First attempts to introduce SIF's for different types of cracked bodies were performed analytically using collocation method, asymptotic methods, weight function methods, singular integrals. This solutions of SIF's were archived in handbooks, like Tada et al. (1985), Murakami (19987). The numerical determination of SIF's are reviewed in Ingraffea & Wawrzynek (2003) and Kuna (2010). One of the key issue is to extract the SIF's from the numerical analysis results (displacements, strains, stresses, energy), based on displacement correlation, J-integral, modified crack closure methods. Almost all experimental stress analysis techniques were adopted to estimate the SIF's for cracked bodies.

This paper presents a simple experimental technique the mark tracking combined to displacement correlation as a simple methodology for teaching students how to find the SIF's for cracked bodies.

**Nomenclature**

- a crack length
- B specimen thickness
- $K_I, K_{II}$  mode I and mode II stress intensity factors
- P applied load
- r polar radius
- S span
- W specimen width
- u, v, w displacements
- $\theta$  polar angle
- $\mu$  shear modulus
- $\nu$  Poisson ratio

**2. Displacement Correlation Methods**

The Displacement Correlation (DC) methods are simple and easy to extract SIF's from a Finite Element Analysis (FEA) of a cracked body, Ingraffea & Wawrzynek (2003), or from experimental data. The nodal displacements represent primary FEA results and during years different approaches were propose to estimate the SIF's from the displacement field. Chan et.al. (1970) considering plane strain assumption and triangular elements at the crack tip, Fig. 2.a proposed the evaluation of SIF's with the relations:

$$K_I = \frac{\mu\sqrt{\pi}(v_b - v_a)}{\sqrt{2r}(1 - \nu)}, K_{II} = \frac{\mu\sqrt{\pi}(u_b - u_a)}{\sqrt{2r}(1 - \nu)}, K_{III} = \frac{\mu\sqrt{\pi}(w_b - w_a)}{\sqrt{2r}} \tag{1}$$



with  $\mu$  the shear modulus,  $\nu$  the Poisson ratio,  $r$  the distance from the crack tip to the corresponding node and  $u_i, v_i, w_i$  are the nodal displacements of point  $i$ , measured on  $x, y, z$  axis. For the case of plain stress  $\nu$  is replaced by  $\nu/(1+\nu)$ .

Most accurate results could be obtained using quarter point crack tip elements, Fig.2. b.

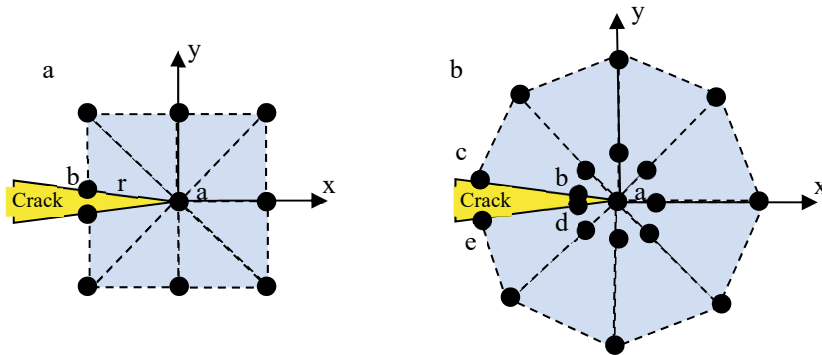


Fig. 2. (a) triangular elements; (b) quarter point crack tip elements.

The SIF's expressions according with Shih et al. (1976) and Tracey (1977) are:

$$K_I = \frac{\mu\sqrt{\pi}[4(v_b - v_d) + v_e - v_c]}{\sqrt{2r(1-\nu)}}, K_{II} = \frac{\mu\sqrt{\pi}[4(u_b - u_d) + u_e - u_c]}{\sqrt{2r(1-\nu)}} \quad (2)$$

The use of displacement correlation technique is simply and allow the separation of different mode of fracture. However, to obtain accurate results a highly refine mesh at the crack tip is necessary and care in selecting the nodes from crack singularity zone. Another alternative is to compute an apparent stress intensity factor  $K_{AP}$  for a series of points approaching the crack tip, to interpolate the results and then extrapolate at the crack tip for  $r \rightarrow 0$ . The processing of data is based on the displacement field near crack tip for a mixed mode load:

$$u = \frac{K_I}{4\mu} \sqrt{\frac{r}{2\pi}} \left[ (2\kappa - 1) \cos \frac{\theta}{2} - \cos \frac{3\theta}{2} \right] - \frac{K_{II}}{4\mu} \sqrt{\frac{r}{2\pi}} \left[ (2\kappa + 3) \sin \frac{\theta}{2} + \sin \frac{3\theta}{2} \right] \quad (3)$$

$$v = \frac{K_I}{4\mu} \sqrt{\frac{r}{2\pi}} \left[ (2\kappa + 1) \sin \frac{\theta}{2} - \sin \frac{3\theta}{2} \right] + \frac{K_{II}}{4\mu} \sqrt{\frac{r}{2\pi}} \left[ (2\kappa - 3) \cos \frac{\theta}{2} + \cos \frac{3\theta}{2} \right]$$

with  $(r, \theta)$  the polar coordinates,  $\mu$  the shear modulus,  $\nu$  the Poisson ratio and  $\kappa=(3-\nu)/(1+\nu)$  for plane stress, respectively  $\kappa=3-4\nu$  for plane strain.

In order to practically apply this technique the displacements on a certain direction  $\theta$ , along a radial line for different distances  $r$  (Fig 3.a) are selected and the apparent SIF's are calculated:

$$K_I \begin{Bmatrix} (2\kappa - 1) \cos \frac{\theta}{2} - \cos \frac{3\theta}{2} \\ (2\kappa - 1) \sin \frac{\theta}{2} - \sin \frac{3\theta}{2} \end{Bmatrix} = 4\mu \sqrt{\frac{2\pi}{r}} \begin{Bmatrix} u \\ v \end{Bmatrix} \quad (4)$$

$$K_{II} \begin{Bmatrix} -(2\kappa + 3) \sin \frac{\theta}{2} - \sin \frac{3\theta}{2} \\ (2\kappa - 3) \cos \frac{\theta}{2} + \cos \frac{3\theta}{2} \end{Bmatrix} = 4\mu \sqrt{\frac{2\pi}{r}} \begin{Bmatrix} u \\ v \end{Bmatrix}$$

Then an interpolation is performed and the value of SIF's is obtained by extrapolation at the crack tip ( $r \rightarrow 0$ ), Fig.3.b.

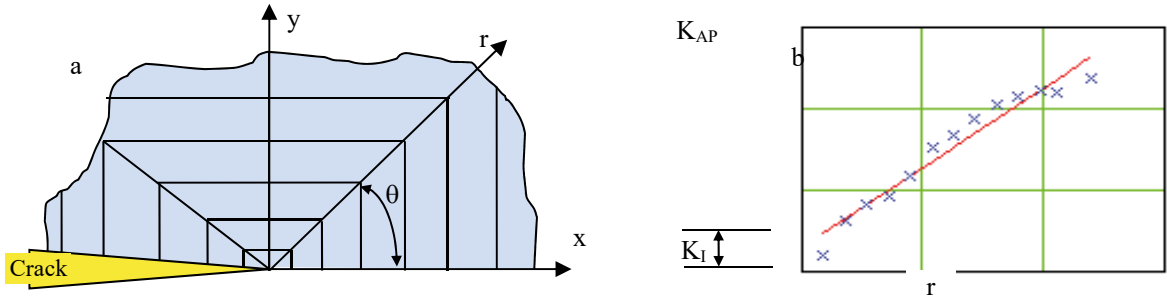


Fig. 3. (a) nodes collected on r direction; (b) extrapolation of apparent SIF at the crack tip.

### 3. Mark Tracking (MT) Techniques

The principle of the method is based on the comparison between two images acquired during the test, before and after deformation Bretagne et al. (2005), Barranger et al. (2013), Pop O. et al. (2013). By comparing the two images, the algorithm of method detects the local displacements in x and y-directions. The principle of the method summarized in Fig. 4. The displacement of each mark is the translation vector  $(u_1, u_2=v)$  in  $x_1$  and  $x_2=y$  directions of the centre of gravity.

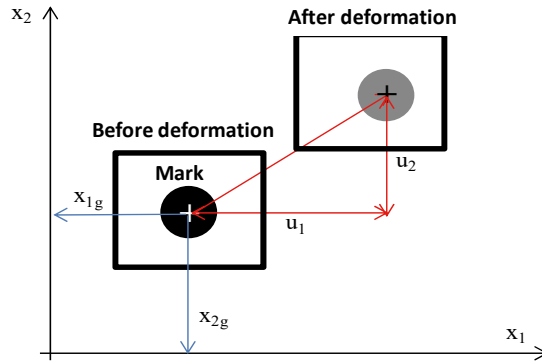


Fig. 4. Principle of Mark Tracking Techniques

According with the principle of method, for the experimental measurements several black marks are positioned on the surface of sample. In our study the marks tracking method allows too definite limits of study zone. The black marks are positioned manually on the specimen surface. Moreover, in order to have a good contrast the black marks are positioned on the white background painted on the specimen surface.

It should be also mentioned that this technique can be usually coupled with the finite element method. In fact, the mark positioned on the surface of specimen may be associated with the nodes of the finite element mesh. As shown in Fig. 4, using the mark positioned on the surface of our sample it is possible to create the meshes with the triangular or the quarter point crack tip elements.

### 4. Experimental determination of SIF's

A relatively simple procedure to experimentally determine the SIF's is to combine the Mark Tracking technique, which allows the determination of displacements, with the DC method for estimating the SIF's.

A Single Edge Notch Bend (SENB) specimen was employed for experimental tests loaded in Three Point Bending. The specimen is made of rigid polyurethane foam with a density of  $145 \text{ kg/m}^3$ , used in civil engineering for thermal isolation. The elastic and mechanical properties of this material are presented in Marsavina et al. (2014, 2015) with a Poisson ratio  $\nu=0.302$ , shear modulus  $\mu=40.62 \text{ MPa}$ , tensile strength  $\sigma = 1.87 \text{ MPa}$  and mode I fracture toughness  $K_{IC}= 0.131 \text{ MPa m}^{0.5}$ . The analytical solution for the mode I SIF is provided in ASTM D5045 (1999):

$$K_I = \frac{P}{BW^{1/2}} f_I\left(\frac{a}{W}\right) \tag{5}$$

$$f_I\left(\frac{a}{W}\right) = 6\left(\frac{a}{W}\right)^{1/2} \frac{1.99 - \left(\frac{a}{W}\right)\left(1 - \frac{a}{W}\right)\left[2.15 - 3.93\frac{a}{W} + 2.7\left(\frac{a}{W}\right)^2\right]}{\left[1 + 2\left(\frac{a}{W}\right)\right]\left(1 - \frac{a}{W}\right)^{3/2}} \tag{6}$$

with  $P$  load,  $B$  specimen thickness,  $W$  width of the specimen,  $a$  crack length and  $f_I(a/W)$  non-dimensional stress intensity factor depending on the crack length. For  $a=19.3$  mm,  $W=50.2$  mm,  $B=25.5$  mm and applied load of 100 N the mode I SIF is  $K_{I,an}=4.198$  MPa mm<sup>0.5</sup>.

On the specimen surface marks were drawn on radial directions from crack tip with a special marker, Fig. 5. The test was performed at room temperature, in displacement control, with a loading speed of 0.5 mm/s, up to 100 N. This load value is lower than the fracture load, and on the linear part of the load-displacement curve.

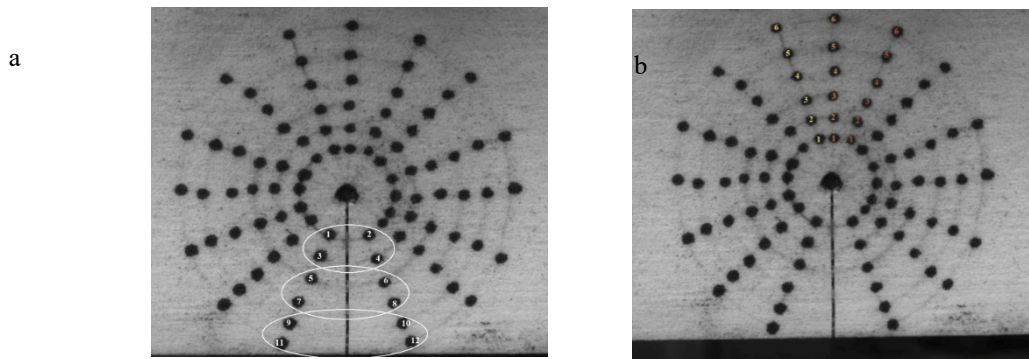


Fig. 5. Marks used for SIF valuation (a) eq. (2), (b) eq. (4)

A USB uEye SE CMOS camera (resolution: 3840 x 2748) with a Pentax 12.5–75 mm lens and a LED light source was used to record 2 fps during the test. In the present study, the Mark Tracking method was performed by using Deftac developed by PEM team of Pprim Institut of Poitiers. Five combinations of marks were considered (like 1-2-3-4), the displacements of each mark were measured and rel. (2) was applied to determine SIF's, Fig.5.a. A comparison of results with the analytical value  $K_{I,an}$  is presented in Fig. 6. It could be observed that the closest values of the  $K_I$  comparing with the analytical value (green line in Fig. 6) were obtained for the first two mark combinations 1-2-3-4 and 3-4-5-6. This is in agreement with other experimental techniques, like photoelasticity and thermoelasticity, which indicates that the stress singularity zone is between 0.2 to 0.5 crack length (red lines in Fig. 6).

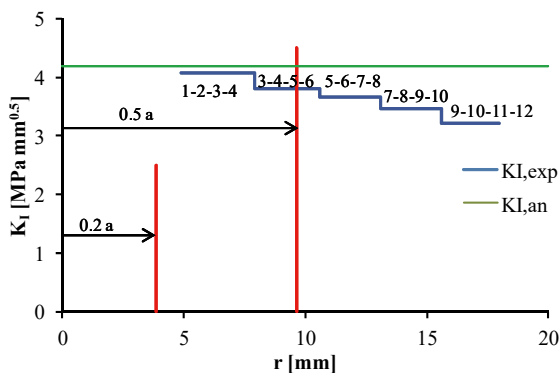


Fig. 6. SIF results based on eq. (2)

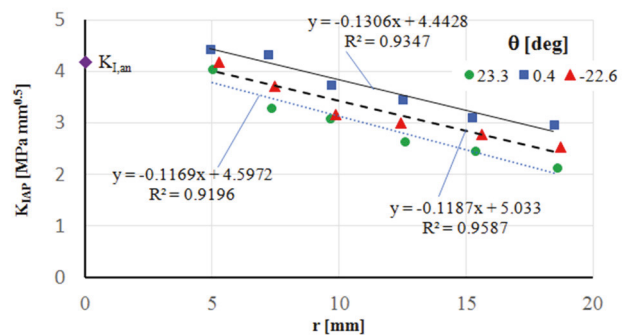


Fig. 7. SIF results based on eq. (4)

The results of the extrapolation method are shown in Fig. 7. The interrogation of displacements was performed on three directions corresponding to  $\theta = 23.3^0$ ,  $0.4^0$  and  $-22.6^0$ . By applying eq. (4) the apparent SIF's were calculated for 6 marks on each direction, then the results were interpolated and extrapolated at the crack tip. The obtained experimental values of  $K_I$  are 4.597 MPa mm<sup>0.5</sup> for  $\theta = 23.3^0$ , 4.442 MPa mm<sup>0.5</sup> for  $\theta = 0.4^0$ , and 5.033 MPa mm<sup>0.5</sup> for  $\theta = -22.6^0$ . It could be seen that all directions overestimates the value of  $K_I$ , while the smallest error 5.8% was obtained for  $\theta = 0.4^0$ .

## 5. Conclusions

Mark tracking technique associated with displacement correlation method represent a simple, suggestive and relatively precise methodology to estimate mode I stress intensity factors. The accuracy of the two methods are in the limit of experimental stress analysis techniques up to 15% to analytical value for the first three nodes combinations (1-2-3-4, 3-4-5-6 and 5-6-7-8) when applying eq. (2), respectively up to 10 % for two directions for extrapolation method ( $\theta = 23.3^0$  and  $0.4^0$ ).

The advantages of combining MT and DC method are: easy to employ, not need special specimen surface treatment, only creating of some marks, and equipments a Digital Camera is enough. The methodology could be applied also to mixed mode (I and II) loading. In order to increase the accuracy of the method an over deterministic method based on nonlinear least square combined with Newton-Raphson could be employed the same like in the case of strain gauges or Digital Image Correlation (Yoneyama, 2006).

## Acknowledgement

This work was partially supported by a grant of the Romanian Ministry of Research and Innovation, CCCDI – UEFISCDI, project number PN-III-P1-1.2-PCCDI-2017-0391 / CIA\_CLIM - *Smart buildings adaptable to the climate change effects*, within PNCDI III”.

## References

- ASTM D5045-99. Standard test methods for plane-strain fracture toughness and strain energy release rate of plastic materials.
- Barranger, Y., Doumalina P., Dupre J.C., Germaneau, A., Hedan, S., Valle V., 2009. Evaluation of three-dimensional and two-dimensional full displacement fields of a single edge notch fracture mechanics specimen, in light of experimental data using X-ray tomography, *Engineering Fracture Mechanics*, 76, 2371-2383.
- Bretagne, N., Valle, V., Dupre, J.C., 2005. Development of the marks tracking technique for strain field and volume variation measurements, *NDT&E International*, 38, 290–298.
- Chen, C.-S., Tuba, I.S., Wilson, W.K., 1970. On the finite element method in linear fracture mechanics, *Engineering Fracture Mechanics*, 2, 1-17.
- Dally, J.W., Sanford, R.J., 1985. Strain Gage Methods for Measuring the Opening Mode Stress Intensity Factor,  $K_I$ , Proc. 1985 SEM Spring Conf. on Exp. Mech., 851-860.
- Dally, J.W., Berger J.R., 1986. A Strain Gage Method for Determining  $K_I$  and  $K_{II}$  in a Mixed Mode Stress Field, Proc. 1986 SEM Spring Conf. on Exp. Mech., 603-612.
- Ingraffea, A.R., Wawrzynek, P.A., 2003. Finite Element Methods for Linear Elastic Fracture Mechanics in Comprehensive Structural Integrity, Eds. Milne, O., Ritchie, R.O, Karihaloo, B., Elsevier Science, Amsterdam, 1-88.
- Kuna, M., 2010. Finite Elements in Fracture Mechanics. Theory-Numerics-Applications, Springer, Dordrecht.
- Marsavina, L., Constantinescu, D.M., Linul, E., Apostol, D., Voiconi, T., Sadowski, T., 2014. Refinements on fracture toughness of PUR foams, *Engineering Fracture Mechanics*, 129, 54-66.
- Marsavina, L., Constantinescu, D.M., Linul, E., Voiconi, T., Apostol, D., 2015. Shear and mode II fracture of PUR foams, *Engineering Failure Analysis*, 58, 465-476.
- Murakami, Y., 1987. Stress Intensity Factors Handbook, 1st edition, Pergamon Press
- Owen, D.R.J., Fawkes, A.J., 1983. Engineering Fracture Mechanics: Numerical Methods and Applications, Pineridge Press, Swansea.
- Pop O., Dubois F., Absi J. 2013. J-integral evaluation in cracked wood specimen using the mark tracking method, *Wood Science and Technology*, 47 (2), 257-267.
- Yoneyama, S., Morimoto, Y., Takashi, M., 2006. Automatic evaluation of mixed mode stress intensity factors utilizing Digital Image Correlation, *Strain*, 42(1), 21-29.
- Saouma, S.E., 2007. Lecture Notes in Fracture Mechanics, Boulder.
- Shih, C.F., Delorenzi, H.G., German, M.D., 1976. Crack extension modeling with singular quadratic isoparametric elements, *International Journal of Fracture*, 1, 647-651.
- Tada, H., Paris, P., Irwin, G., 1985. The Stress Analysis of Cracks Handbook, Second Edition, St. Louis.
- Tracey, D.M., 1971. Finite elements for determination of crack tip elastic stress intensity factors, *Engineering Fracture Mechanics*, 3, 255-256.